第 23 回
核燃焼プラズマ
統合コード研究会

23rd Burning Plasma Simulation Initiative (BPSI) Meeting

日時：2026 年 1 月 7 日(水)－9 日(金)
場所：九州大学筑紫キャンパス
総合研究棟 C-cube 1 階筑紫ホール、
応用力学研究所 2 階大会議室
および オンライン

(Ver. 2, 2026 年 3 月 3 日発行)

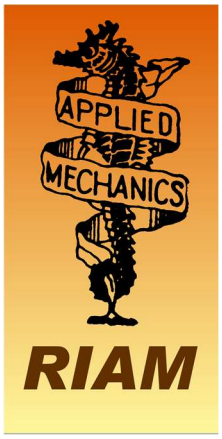

合同会合

閉じ込め・輸送に関する研究会 2025

Workshop on Plasma Confinement and Transport 2025

第 23 回核燃焼プラズマ統合コード研究会

23rd Burning Plasma Simulation Initiative (BPSI) Meeting

(Ver.4.2)

日時：2026 年 1 月 7 日(水)－9 日(金)
場所：九州大学筑紫キャンパス および オンライン
7 日(水) 12:30 – 15:35 応用力学研究所 2 階 大会議室
7 日(水) 15:55 – 19:00、8 日(木)、および 9 日(金)　総合研究棟 C-cube 1 階 筑紫ホール
(7 日の途中に建物を移動する必要がございます)
Note: We will need to move the building during the day 7th Jan.

・1 月 7 日(水)

12:30 – 12:55　会議登録 Registration
12:55 – 13:00　事務連絡 Business announcement

(閉じ込め・輸送に関する研究会 2025)
「応用力学研究所 2 階 大会議室」にて

(座長：前山)
13:00 – 13:05　はじめに　　前山 伸也 (核融合研) Opening remark
13:05 – 13:30　講演 1-1　　釼持 尚輝 (核融合研)
非局所輸送におけるメディエータとして作用する乱流の実験的同定
13:30 – 13:55　講演 1-2　　伊藤 公孝 (中部大)
輸送ヒステリシスと亜臨界乱流
13:55 – 14:15　講演 1-3　　講演取り消し canceled

14:15 – 14:25　休憩 break

(座長：釼持)
14:25 – 14:50　講演 1-4　　前山 伸也 (核融合研)
例外点における電子温度勾配不安定性とイオンバーンシュタイン波の結合
14:50 – 15:15　講演 1-5　　河内 裕一 (名大)
逆磁場ピンチプラズマにおけるトロイダル帯状流と乱流の時空間ダイナミクス
15:15 – 15:35　講演 1-6　　古田原 拓実 (日大)
トカマクプラズマにおける ELM バーストを伴う抵抗性ドリフトバルーニングモード乱流のモード縮約

15:35 – 15:55　筑紫ホールへ移動、休憩 move to Chikushi Hall, break

以降、「総合研究棟 C-cube 1 階 筑紫ホール」にて

(座長：河内)
15:55 – 16:20　講演 1-7　　永岡 賢一 (核融合研)
CHD プラズマ実験計画
16:20 – 16:45　講演 1-8　　小林 達哉 (核融合研)
磁場閉じ込めプラズマ速度分布関数のベイズ推定
16:45 – 17:10　講演 1-9　　米田 亮太 (NTT 研究所)
Decision Transformer を用いたトカマクプラズマ制御と運転安定性の予備的評価

17:10 – 17:20　休憩 break

(座長：小林(達))
17:20 – 17:45　講演 1-10　　高部 英明 (阪大)
レーザー核融合統合コードの物理「Physics integrated code for laser fusion」
17:45 – 18:10　講演 1-11　　東井 和夫 (核融合研)
EAST トカマクプラズマにおける低域混成波電流駆動(LHCD)電力変調と周辺局在化モードに対する SOL 幅とダイバータストライク線位置の過渡応答
18:10 – 18:35　講演 1-12　　渡邉 智彦 (名大)
マルチスケール乱流相互作用と捕捉電子モードへの同位体効果
18:35 – 19:00　講演 1-13　　徳沢 季彦 (核融合研) online
クロススケール乱流間相互作用に関する LHD 実験結果報告と CHD での計画

19:00　散会

・1 月 8 日(木)
「総合研究棟 C-cube 1 階 筑紫ホール」にて

(ITPA セッション)

(座長：相羽)
9:00 – 9:05　講演 2-1　吉田 麻衣子 (量研) online
趣旨説明
9:05 – 9:30　講演 2-2　今寺 賢志 (京大)
近年のグローバルジャイロ運動論シミュレーション研究の動向
9:30 – 9:55　講演 2-3　本多 充 (京大)
粒子輸送を考慮した定常輸送コード GOTRESS の機能拡張
9:55 – 10:20　講演 2-4　成田 絵美 (京大)
プラズマ周辺部の乱流揺動解析と輸送モデル開発に関する共同活動

10:20 – 10:30　休憩 break

(座長：本多)
10:30 – 10:55　講演 2-5　相羽 信之 (量研)
ITPA 周辺ペデスタル TG での最近の話題について
10:55 – 11:20　講演 2-6　小林 政弘 (核融合研)
LHD のデタッチメント運転時の閉じ込めプラズマ挙動
11:20 – 11:35　講演 2-7　吉田 麻衣子 (量研) online
ITPA Special issue の作成中にでた輸送研究の重要課題

11:35 – 11:50　休憩 break

11:50 – 13:30　ポスター講演 Poster
(筑紫ホール前ロビー、コアタイム：奇数番号 11:50-12:40 偶数番号 12:40-13:30)

13:30 – 13:45　休憩 break

(閉じ込め・輸送に関する研究会 2025)

(座長：今寺)
13:45 – 14:10　講演 2-8　瀬戸 春樹 (量研)
Turbulence Burst in Resistive-Drift-Ballooning Mode Driven ELM Crash
14:10 – 14:35　講演 2-9　西村 征也 (量研)
平衡フローの駆動するバルーニングモード乱流のバーストダイナミクス

(核燃焼プラズマ統合コード研究会)

(座長：村上)

14:35 – 15:00　講演 3-1　　Gyungjin Choi (KAIST)
A theory of fast ion population on ExB staircase stability
15:00 – 15:25　講演 3-2　　Aaron Froese (General Fusion)
Modeling and reconstruction of plasma compression in the LM26 device at General Fusion
15:25 – 15:45　講演 3-3　　安齋 亮慶 (京大)
Consideration of the operational scenario planning with Bayesian network

15:45 – 15:55　休憩 break

(特別セッション)

(座長：糟谷)
15:55 – 16:05　趣旨説明　　糟谷 直宏 (九大)
Introduction
16:05 – 17:05　特別講演 1　　矢木 雅敏 (量研)
Past, present and future of Burning Plasma Simulation Initiative (BPSI)

17:05 – 17:25　集合写真 group photo、休憩 break

(核燃焼プラズマ統合コード研究会)

(座長：糟谷)
17:25 – 17:50　講演 3-4　　二谷 辰平 (量研)
3D non-linear simulations of MHD instabilities in magnetically confined plasma
17:50 – 18:15　講演 3-5　　徳永 晋介 (量研)
Vision and current status of the informatic research center for fusion energy research
18:15 – 18:40　講演 3-6　　横山 雅之 (核融合研)
Report of IMEG

18:40　散会

19:20 – 21:20　懇親会 (独楽蔵 JR 大野城駅近)

・1 月 9 日(金)

「総合研究棟 C-cube 1 階 筑紫ホール」にて

(核燃焼プラズマ統合コード研究会)

(座長：成田)

9:00 – 9:25　講演 4-1　沼波 政倫 (核融合研)
Effective dynamics on a reduced space for plasma turbulent transport

9:25 – 9:50　講演 4-2　佐々木 真 (日大)
Bifurcation of turbulence trapping by zonal flows near density limit

9:50 – 10:10　講演 4-3　Huiwon Chung (SNU)
Development of a data-driven neural network model for electron thermal transport in NSTX

10:10 – 10:20　休憩 break

(座長：沼波)

10:20 – 10:45　講演 4-4　相羽 信行 (量研)
H-mode operation scenarios in JT-60SA initial research phase predicted by integrated core-pedestal-SOL/divertor simulation

10:45 – 11:10　講演 4-5　成田 絵美 (京大)
Development of models for time-dependent simulations of the pedestal region

11:10 – 11:35　講演 4-6　藤田 隆明 (名大)
Study on plasma operation conditions in the FAST device with TOTAL code

11:35 – 12:00　講演 4-7　福山 淳 (京大)
Recent progress of integrated code TASK

12:00 – 12:45　昼休み Lunch break

(座長：藤田)

12:45 – 13:10　講演 5-1　Apiwat Wisitsorasak (KMUTT)
Development of core-SOL-divertor model for simulating tokamak plasmas with impurities

13:10 – 13:35　講演 5-2　糟谷 直宏 (九大)
Transport simulation of impurities in nuclear fusion tokamak devices by using integrated code TASK

13:35 – 14:00　講演 5-3　登田 慎一郎 (核融合研)
Modeling of turbulence transport by dissipative trapped electron and ion temperature gradient modes in tokamak plasmas

14:00 – 14:25　講演 5-4　河村 学思 (量研)
Numerical transport study of charge-exchange neutrals in fusion devices

14:25 – 14:35　休憩 break

(座長：河村)

14:35 – 15:00　講演 5-5　　村上 定義 (京大)
Simulation study of ECH multiple resonance heating and energetic electron generation in the QUEST spherical tokamak

15:00 – 15:25　講演 5-6　　奴賀 秀男 (核融合研) online
NBCD simulation in the LHD

15:25 – 15:50　講演 5-7　　杉山 翔太 (量研)
Approximate analytical expression for knock-on tail

15:50 – 16:10　講演 5-8　　Min Ki Jung (SNU)
Global gyrokinetic study of KSTAR disruptive plasmas

(Session Leader：村上)

16:10 – 16:25　議論 Discussion

16:25 – 16:30　事務連絡 Business announcement

16:30　散会

16:30 – 17:00　個別の議論 Discussion

Poster number

Plasma Confinement and Transport Workshop 2025 / 23nd BPSI meeting (2026)

P01 川村祐介(九大) Y. Kawamura
Transport simulations using the integrated code TASK and a gyrofluid model

P02 田中晴也(名大) S. Tanaka
Evaluation of the effects of electron cyclotron waves or negative-ion-based neutral beam injection on tungsten transport characteristics in JT-60U plasmas

P03 平位元(名大) G. Hirai
Development of a simple analysis module for electron cyclotron current drive

P04 坂本孝介(九大) K. Sakamoto
Effect of resonance surface position on density flattening in reduced MHD simulation of tokamaks

P05 安井和寿(名大) K. Yasui
A comparative study on determining methods for multi-variable PID control gains of JA DEMO using TOTAL

P06 太田有哉(兵庫県立大) Y. Ohta
Study on image reconstruction of lensless microwave holography in a linear plasma device

P07 中田洋輝(兵庫県立大) H. Nakata
Estimation of fast ion density distribution in fusion plasmas using FIDASIM data and CNN

P08 林瀚清(九大) H. Lin
Synthetic diagnostics of tokamak turbulence spectrum by numerical PCI

P09 岡林 秀明(京大) H. Okabayashi
平行方向磁場揺動のマイクロティアリングモードへの影響

P10 河津 智也(京大) T. Kawadu
捕捉電子不安定性による乱流輸送への Shafranov-shift 効果

P11 徳山 和映(京大) K. Tokuyama
電磁乱流輸送のプラズマサイズスケーリング

P12 猪塚 祐(京大) T. Izuka
臨界勾配近傍における乱流輸送のヒステリシスを記述する簡約化モデル

P13 奥和田 輝(九大) H. Okuwada
CO_2レーザー干渉計を用いた LHD プラズマの密度限界到達過程の解析

Past, present and future of Burning Plasma Simulation Initiative (BPSI)

M. Yagi

National Institutes for Quantum and Radiological Science and Technology,
Rokkasho Fusion Institute, Rokkasho, Aomori, Japan
Research Institute for Applied Mechanics, Kyushu University, Kasuga, Fukuoka, Japan

1. Introduction

The fusion plasma such as ITER and DEMO indicates highly autonomous nature. It is open system including multi-scale and multi-physics phenomena. The prediction of burning state and development of burn control method are keys to realize fusion power plant. For this purpose, it is necessary to simulate self-contained time evolution of whole discharge, i.e., startup, sustainment, abrupt event such as disruption and termination of core, edge and divertor plasmas. Figure 1 shows the range of time and spatial scales of the phenomena in fusion plasmas which includes the wide range of time scale from 100 GHz to 1,000 s and of special scale from 10 μm to 10m. The single simulation code which covers whole time and special scale could be developed in principle, but it is not realistic. The practical approach is the integration of multiple codes which describe various physical phenomena. So far, the first principle simulations are also performed, however, to treat multi-scale and multi-physics phenomena are limited due to the capability of supercomputer. Quantitative prediction on burning plasmas as well as development of control methods are strategically important for ITER and DEMO to develop operation scenario and so on. For this purpose, the Burning Plasma Simulation Initiative (BPSI) has been established in 2002, which is the collaboration activity between domestic universities, NIFS, QST (JAEA) etc. Table I shows history of BPSI and related US-Japan JIFT workshops.

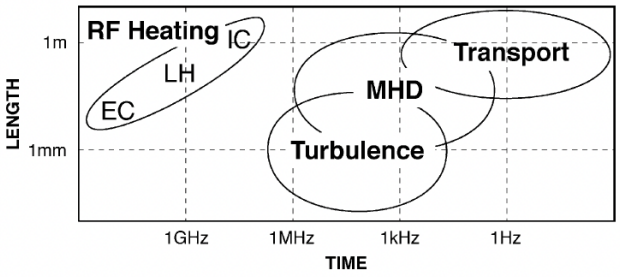

Fig.1 The range of time and spatial scales of the phenomena in fusion plasmas (cited from Fig.1 in Ref. [1]).

Date	Event
07/12/2002	Fusion Simulation Project (US)

07/31/2002	BPSI preliminary meeting at NIFS
11/01/2002	BPSI mini workshop at Kyoto University
11/28/2002	BPSI discussion forum in JSPF informal meeting II at Inuyama
01/07/2003	BPSI mini workshop at Kyoto University
12/15-17/2003	US-Japan JIFS WS on "Theory-Based Modeling and Integrated Simulation of Burning Plasmas" at Kyoto University
03/17-18/2003	BPSI mini workshop at RIAM Kyushu University
05/01/2003	BPSI mini workshop at Naka Institute JAEA
07/31-08/01/2003	1st BPSI meeting at Kyoto University
03/18-19/2004	2nd BPSI meeting at RIAM Kyushu University
9/21-24/2004	US-Japan JIFS WS on "Theory-Based Modeling and Integrated Simulation of Burning Plasmas" at Princeton Plasma Physics Laboratory
9/13-15/2005	US-Japan JIFS WS on "Integrated Modeling of Multi-Scale Physics in Fusion Plasmas" at Kyushu University
From 2nd meeting, annual BPSI meeting has been held as research meeting of RIAM Kyushu University. At present, BPSI is 23 years old.	

Table I History of BPSI and related US-Japan JIFT workshops

2. Present status of BPSI

The progress of BPSI can be seen in Ref. [2]. Also, BPSI is tightly coupled with Numerical Experiment of Tokamak (NEXT) project [3]. Figure 2 shows various physical modules for integrated transport simulation. The first principle simulation codes are partially coupled with transport modules, which can improve the prediction capability, although it requires computational costs. One example is a self-consistent integrated simulation model of core and scrape-off-layer (SOL)/divertor transport [4]. This model enables the user to investigate operational scenarios with compatible high-confinement core plasmas and detached divertor plasmas. A 1.5D core code TOPICS-IB and a 2D divertor code SONIC are successfully coupled using a Multiple Program Multiple Data parallel computing system. This integrated code, which can include Monte-Carlo models for neutrals and impurities, provides efficient plasma/neutral

simulations. The dynamic simulation for the L/H transition in JT-60SA is carried out by this integrated code using a current-diffusive ballooning mode (CDBM) transport model that includes the E×B shearing effect.

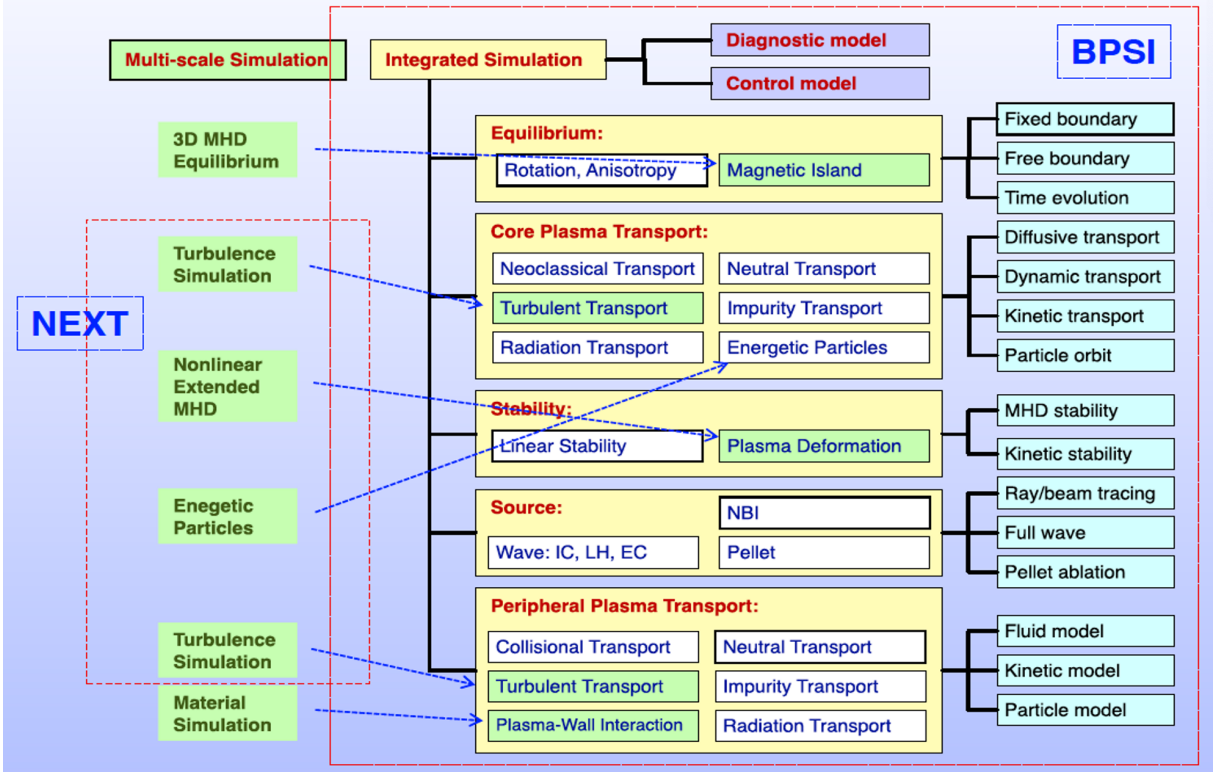

Fig.2 Various physical modules for integrated transport simulation. The red thick box indicates modules for integrated simulation such as equilibrium, core plasma transport, stability, source and peripheral plasma transport etc. The multi-scale simulation is performed by the first principle simulation codes, which will be partially coupled with transport modules.

3. Future prospect of BPSI

Future prospect of BPSI is discussed in Ref. [5]. Especially, 1) real time plasma control, 2) robust transport simulation coupled with advanced turbulence model such as TGLF, 3) surrogate model of TGLF for accelerated simulation, 4) kinetic integrated transport model, etc. should be developed in future. Figure 3 shows computer resources required by Fusion Simulation Project (FSP) cited from Figure II.1 in Ref. [6]. The red circle shows that topics proposed in 2002 have been already attained in 2025. According to IAEA FEC 2025 [8], we found that 1) whole device simulation, 2) integrated impurity transport simulation, 3) JOREK disruption simulation, 4) digital twin were presented which correspond to 1) GK Full Torus, 2)

Virtual Edge, 3) Virtual Disruption, 4) Burning Plasmas Integrated Simulation in FSP 2002, respectively.

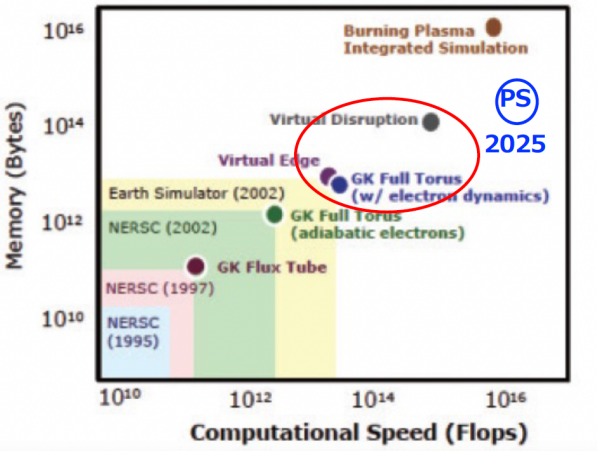

Fig.3 Computer resources required by Fusion Simulation Project cited from Figure II.1 in Ref. [6]. PS indicates Plasma Simulator supercomputer in QST & NIFS which has been operating since July 2025 [7].

4. Summary and discussion

BPSI is national integrated modeling activity (~2002) in Japan. Objective is establishment of quantitative description of burning plasmas in ITER. NEXT is numerical experiment of Tokamak project (~1996) in JAERI, JAEA and QST. Objective is understanding complex properties of fusion plasmas and prediction physical processes in next generation Tokamaks such as JT60SA, ITER and DEMO. These projects are two sides of the same coin. AI/ML is a new ingredient to join both projects as well as GPU simulation technology. These elements will play a key role to construct digital twin of DEMO.

Acknowledgements

The computations were carried out on Helios, Japan Fusion Reactor Simulator 1 (JFRS-1), Plasma Simulator (PS) and SGI HPE8600 supercomputer at QST and JAEA. This work was supported in part by the Collaborative Research Program of Research Institute for Applied Mechanics, Kyushu University (2025CR-FP-23). The author (M. Y.) acknowledges all collaborators for fruitful discussions and supports.

Reference

[1] A. Fukuyama and M. Yagi, “Burning Plasma Simulation Initiative and Its Recent Progress”, J. Plasma Fusion Res. Vol.81, No.10 (2005) 747-754.

[2] N. Hayashi, A. Fukuyama, S. Murakami, M. Yokoyama and T. Fujita, “Simulation of Magnetically Confined Fusion Plasma by Integrated Code and its Prospect”, J. Plasma Fusion Res. Vol.95, No.9 (2019) 421-426.

[3] M. Yagi, “NEXT Project and Theory/Simulation Research in BA CSC”, RIST News, No. 49 (2010). Also, see https://www.qst.go.jp/site/jt60/5281.html

[4] M. Yagi, K. Shimizu, T. Takizuka, M. Honda, N. Hayashi, K. Hoshino, and A. Fukuyama, “Simulation Study of L/H Transition with Self-Consistent Integrated Modelling of Core and SOL/Divertor Transport”, Contrib. Plasma Phys. Vol.52 Issue 5-6 Special Issue:13th International Workshop on Plasma Edge Theory in Fusion Devices (2012) 372-378.

[5] M. Honda, E. Narita, N. Hayashi, M. Yagi, A. Fukuyama, S. Murakami, M. Yokoyama, and T Fujita, “Future Prospects of Integrated Code Development”, J. Plasma Fusion Res. Vol.95, No.9 (2019) 543-457.

[6] Final Report of the FESAC ISOFS Subcommittee, Dec. 1 (2002).

[7] Plasma Simulator; https://www.qst.go.jp/site/rokkasyo/46853.html

[8] 30th IAEA Fusion Energy Conference (FEC2025), 13–18 October 2025, Chengdu, People’s Republic of China; https://www.iaea.org/events/fec2025

Consideration of the Operational Scenario Planning with Bayesian Network

Akiyoshi Anzai[1)], Emi Narita[1)], Mitsuru Honda[2)], Yuya Morishita[1)] and Sadayoshi Murakami[1)]

[1)] *Department of Nuclear Engineering, Kyoto University, Kyoto 615-8540, Japan*

[2)] *Engineering Education Research Center, Kyoto University, Kyoto 615-8530, Japan*

January 21, 2026

The efficient operation of a fusion reactor requires systematic planning of operational scenarios under control constraints from plasma ramp-up to sustainment. Conventional scenario design relies on expert knowledge and has difficulties in exploring complex control spaces. This study proposes an automated scenario planning framework based on Bayesian Networks (BNs). The framework represents plasma states probabilistically and employs the backcasting function of BNs to infer feasible operational paths from target conditions. Validation using artificial test data shows that the proposed method can generate feasible scenarios that reproduce qualitative temporal trends of ground-truth trajectories, even when the network structure is partially inferred from data. These results suggest that our method provides a practical approach for automated scenario planning of plasmas.

Keywords: Scenario Planning, Bayesian Network, Automated Planning, Fusion Plasma Control

1 Introduction

In the operation of a fusion reactor, it is essential to accurately understand plasma behavior from ramp-up to sustainment of the burning plasma and to control it efficiently throughout these phases. To achieve these processes, planning of the optimal operational scenarios that use effective control parameters is important for improving operational efficiency and reliability. To date, numerous numerical codes have been developed to predict plasma behavior and analyze underlying physical phenomena. Conventional scenario design has typically been performed by combining such simulation codes with predefined objective functions to evaluate operational optimality. For example, a previous study [1] has investigated operational scenarios using the integrated simulation code TOPICS. It aimed to maintain the minimum safety factor above unity, avoid local minima in its spatial distribution, and reduce the heat load on divertor components.

However, conventional scenario building relies on expert knowledge for parameter selection and suffers from the combinatorial explosion arising from high-dimensional control parameter spaces. These problems hinder systematic exploration of optimal operation, particularly when complex plasma state transitions and time-dependent effects must be considered.

In this study, we aim to address these challenges by developing an automated scenario construction framework based on Bayesian Networks (BNs), a class of probabilistic machine learning models [2, 3]. The proposed approach represents internal plasma states and their temporal evolution within a BN, and employs a path-finding algorithm to systematically explore optimal operational paths in the state space. In this paper, we report validation results of the proposed BN-based automated scenario planning method.

author's e-mail: anzai.akiyoshi.47w@kyoto-u.ac.jp

2 Method

BNs enable probabilistic inference over system states and allow backward reasoning from target conditions to the prior states of the previous time step via conditional probabilities. Using the backcasting function of BNs, we could search for any operational paths that meet the control constraints. The aim of using the backcasting function is to control a fusion reactor, avoiding plasma instability. We developed two types of BNs based on the test data: a BN with a correct network structure derived from the equations in 2.1 and a BN with an inferred network structure. The inferred network was developed by the time-series causal discovery code, IEDS-TE [4]. The network structure inferred by IEDS-TE contains misestimated edges and missing causal relations, possibly due to finite sample size and limitations in the causal discovery methods we used. Therefore, we input some edges in the inferred BN to perform probabilistic reasoning. For each BN, we set pseudo edges of the same time dependence to obey constraints of causal relations in backcasting phases. Fig. 1 shows the inferred BN with variables of equations in 2.1 and the pseudo edges. Using these BNs, we employed a greedy algorithm to search for an operational path.

2.1 Artificial Test Data

Here, the simplified equations for making data are written as follows,

$$\begin{aligned} y_{0,t+1} &= 0.2y_{0,t} + x_{0,t-1}^2 + \cos(20\pi t/n) + e_{y_0} \\ y_{1,t+1} &= 0.35y_{1,t} + 0.5y_{0,t} + 0.2x_{1,t-1} + e_{y_1} \end{aligned}, \quad (1)$$

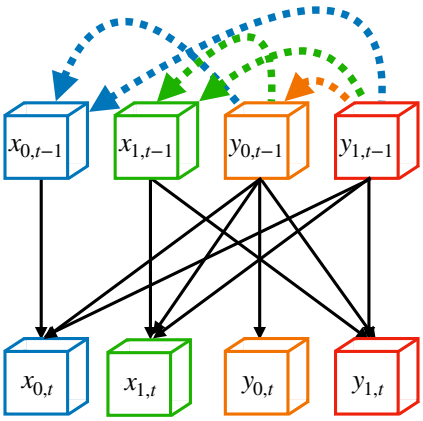

Fig. 1 Inferred BN and pseudo edges. A dashed arrow denotes a pseudo edge. An edge shows the direction of dependence and causality.

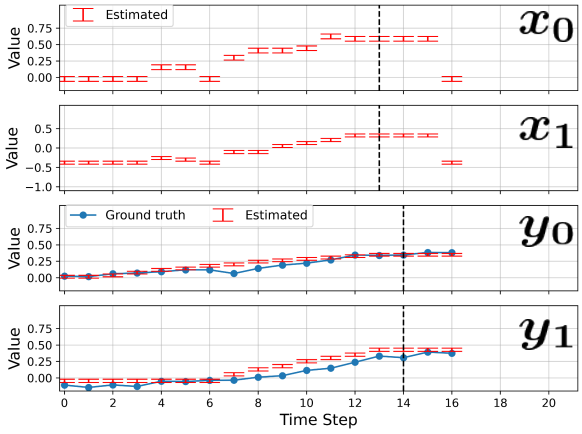

Fig. 2 The validation result. The red bar shows the estimated value, and the blue point denotes the ground truth based on the equation.

where the t denotes the subscript of time and e is a noise term from the uniform distribution $U(-0.025, 0.025)$. n is the sample size of the data. We varied x_0 and x_1 as control variables, mimicking the power input operation from the ramp-up to ramp-down in a fusion reactor. y_0 and y_1 are like physical values affected by the power input. These variables are designed to mimic simplified plasma responses to external power input, including delayed effects relevant to operational control. We collected data 10 times, each with a sample size of 200, to learn BNs.

2.2 Backcasting Algorithm

We developed a greedy backcasting algorithm to find the operational path. Although the proposed algorithm adopts a greedy strategy and does not guarantee global optimality, it is sufficient for validating the feasibility of BN-based backcasting under control constraints in this study. Firstly, we set the goal parameters and initial conditions. Then, we infer each variable from the goal one by one, step by step, using the backcasting functions of the BN. The next state of a variable is determined by the highest probability in the BN within the constraints of finding paths. For example, when we infer $y_{0,t-1}$ of the ramp-up phase, the next state is selected, which has the highest probability, based on the constraint of $y_{0,t-1} \leq y_{0,t}$. After repeating the inference many times, it stops if the set of variables satisfies the initial conditions.

3 Validation of Automated Scenario Planning

We will show the results of the inferred BN. Fig. 2 shows the backcasting scenario and the results of inputting the x parameters of the inferred BN into the equations (1). The red bars denote the backcasting scenario from the ramp-up to sustainment. The former time of the vertical dashed line in the figures is the ramp-up phase, and the time after the line corresponds to the sustainment phase. In both the ramp-up and sustainment phases, the backcasting scenario reproduced the qualitative temporal trends of the ground-truth trajectories generated by the equations. The results of the BN with the correct network performed well. However, the results are omitted due to space limitations. These results indicate that even with imperfectly inferred network structures, the backcasting with BNs can generate feasible operational scenarios that meet control constraints.

4 Conclusion

In this work, we developed BNs and a new algorithm to build operational scenarios. The backcasting scenario planning was evaluated using artificial data that mimicked the operation of a fusion plant. We found that the backcasting scenario planning performed well in this data and demonstrated that BN-based backcasting can construct feasible operational scenarios even when the network structure is partially inferred from data. In the future, we will investigate the constraints on making BNs in detail and apply our method to plan the operational scenario of LHD to avoid radiative collapse.

[1] S. Sugiyama *et al.*, Nucl. Fusion **64**, 076014 (2024).
[2] M. J. Kochenderfer, T. A. Wheeler, and K. H. Wray, *Algorithms for Decision Making* (MIT Press, Cambridge, USA, 2022).
[3] M. Ghallab, D. Nau and P. Traverso, *Automated Planning - theory and practice* (Elsevier, North York, 2004).
[4] A. Anzai *et al.*, "*Development of a Causal Discovery Code IEDS-TE Using a Post-Nonlinear Model and its Application to Time-series Analysis of Fusion Plasmas*", in preparation (2026).

3D non-linear simulations of MHD instabilities in magnetically confined plasma

S. Futatani
National Institutes for Quantum Science and Technology (QST),
Rokkasho, Aomori, 039-3212, Japan

1. Introduction

Magnetohydrodynamic (MHD) instabilities play a central role in limiting plasma performance in magnetic confinement fusion devices and pose a critical challenge for reliable reactor operation. Understanding the non-linear dynamics of these instabilities, as well as developing predictive and control-oriented modeling capabilities, is therefore essential for next-step devices such as ITER and future stellarator-based reactors. The primary motivation of my research is to clarify the physical mechanisms governing instability driven transient events and to provide possible method for their mitigation through advanced non-linear MHD simulations.

In tokamak plasmas operating in the H-mode regime, edge localized modes (ELMs) represent a major concern due to their intense, transient heat loads on plasma facing components [1]. Controlled ELM triggering by pellet injection is one of mitigation strategies, but its application to ITER requires reliable triggering at high frequencies while remaining compatible with strict fuel throughput constraints. Motivated by these requirements, my research has focused on the non-linear physics of pellet-triggered ELM using the JOREK code (www.jorek.eu) [2], incorporating realistic pellet ablation models and comparing with experiments of DIII-D [3], JET [4], ASDEX Upgrade [5]. This work aims to identify the key MHD processes responsible for ELM triggering, assess the resulting power deposition patterns, and determine pellet parameters suitable for ITER-scale plasmas.

In parallel, the research addresses core collapse event in helical plasma, where the inherently three-dimensional magnetic configuration leads to strong non-linear mode coupling. Although stellarators and helical devices avoid large scale disruptions, core collapse events which degrade the confinement have been observed in several devices, including Wendelstein 7-X [6]. These events, often associated with localized toroidal currents and low magnetic shear, remain insufficiently understood. Motivated by this gap, full 3D non-linear MHD simulations using the MIPS code [7] is employed to investigate how localized current-driven modifications of the rotational transform destabilize MHD modes and lead to rapid core density collapse [8].

This manuscript briefly introduces several of my research activities that have contributed to physical understanding of non-linear MHD instabilities in both tokamak and stellarator configurations, with the aim of contributing to the development of robust operational scenarios for future fusion reactors.

2. MHD codes

The JOREK code is a three-dimensional, fully implicit, non-linear extended MHD simulation code developed to model large scale plasma dynamics in toroidal magnetic confinement devices such as tokamaks and stellarators. It employs a high-order finite-element representation on flux-surface-aligned grids in the poloidal plane combined with a toroidal Fourier decomposition, enabling detailed simulation of realistic geometries including X-points, scrape-off layers, and divertor regions. JOREK's numerical solvers are optimized for strongly non-linear evolution, allowing self-consistent time integration of the extended MHD equations with multiple physics extensions such as resistive wall interactions, two-fluid effects, neoclassical flows, and kinetic particle models. The code has been extensively applied to study instabilities relevant to fusion plasma performance and control, including ELMs, disruptions, and their mitigation strategies in current and future devices. A notable capability of JOREK is its pellet ablation model, which

enables the self-consistent simulation of the interaction between pellet ablation and the bulk plasma. In this model, the pellet is represented as a localized, time-varying density source that moves along an arbitral trajectory with fixed velocity, such that the integrated density source is consistent with established scaling laws based on the neutral gas shielding (NGS) ablation model. As the pellet travels into the plasma, the ablation source introduces a localized increase in plasma density, which in turn drives perturbations that evolve with the MHD dynamics.

The MIPS (MHD Infrastructure for Plasma Simulation) code is a Japan-developed MHD simulation framework designed for three-dimensional analysis of macroscopic plasma dynamics in toroidal magnetic confinement devices such as stellarators, tokamaks and RFP devices. MIPS is the extraction of MHD part from MEGA [9] which is a hybrid kinetic-MHD code that extends the MHD modelling capabilities to include kinetic effects of energetic particles. MIPS solves the non-linear MHD equations using finite-difference spatial discretization (typically fourth-order accuracy) and explicit time integration method using Runge-Kutta (typically fourth-order accuracy), with parallelization achieved via the Message Passing Interface (MPI) for efficient execution on high-performance computing platforms. MIPS has been employed to investigate a range of non-linear MHD phenomena relevant to fusion research.

3. Discussion

The primary physics mechanism of triggering is a localized pressure perturbation induced by the pellet ablation that transiently pushes the edge plasma across MHD stability limits. As a pellet penetrates into the pedestal region, it rapidly ablates, creating a dense pellet cloud that expands along magnetic field lines at the local ion sound speed. Meanwhile, parallel heat conductivity which is very fast heat transport along magnetic field lines rapidly reheats the local temperature of the ablated region. This causes a three-dimensionally localized pressure perturbation and local increase in pressure gradient which pressure driven high-n MHD modes (n: toroidal mode number) and initiating an ELM crash earlier than it would occur naturally.

Futatani *et al.* performed the first non-linear MHD simulations of pellet-triggered ELMs using the JOREK extended MHD code. The result of JOREK simulation is that the key parameter controlling pellet-triggered ELMs is the magnitude of the localized pressure perturbation created by the pellet ablation: only when this perturbation exceeds a threshold does the pedestal become unstable and an ELM is triggered. This leads to the existence of a minimum pellet size for triggering at a given injection velocity and plasma state. Smaller pellets do not produce sufficient local pressure increase and therefore do not trigger ELMs in the simulations.

Civit-Bertran *et al.* present three-dimensional non-linear MHD simulations of core density collapse (CDC) events in high-ß plasmas of the Large Helical Device (LHD), using an extended version of the MIPS code that includes anisotropic (parallel and perpendicular) heat conductivity. The goal of the work is to clarify the MHD mechanisms responsible for CDCs and to identify the role of thermal transport during the instability evolution.

The simulations show that CDCs are initiated by the growth of ballooning-like MHD modes localized predominantly on the low-field side of the plasma. During the early linear phase, high-n mode perturbations dominate and produce localized pressure and density distortions without immediately affecting the plasma core. In the non-linear regime, strong mode coupling transfers energy from high-n to low-n modes, leading to a global reformation of the magnetic topology. In this phase, the simulations show that convective transport associated with the plasma velocity becomes comparable to and eventually exceeds conductive transport. This transition coincides with magnetic field stochasticity and marks the onset of the rapid density and pressure collapse.

4. Summary

This work has addressed the non-linear dynamics of MHD instabilities in both tokamak and helical plasmas through comprehensive three-dimensional MHD simulations, with the aim of improving physical understanding and predictive capability for instability-driven transient events in future fusion reactors.

For tokamak H-mode plasmas, the non-linear physics of pellet-triggered ELM was investigated using the extended MHD code JOREK with a self-consistent pellet ablation model. The simulations demonstrate that ELM triggering is controlled by the formation of a localized three-dimensional pressure perturbation generated by pellet ablation. When this localized pressure perturbation exceeds a stability threshold, high-n MHD modes are destabilized and an ELM is triggered prematurely. This mechanism explains the existence of a minimum pellet size for reliable triggering and provides a physics basis for optimizing pellet pacing parameters under the fuel throughput constraints anticipated for ITER. In parallel, CDC events in helical plasmas were studied using full 3D non-linear MHD simulations with the MIPS code. The results show that CDCs are initiated by ballooning-like instabilities localized on the low-field side. While high-n modes dominate the linear phase, non-linear mode coupling transfers energy to low-n modes, leading to magnetic field stochasticization and global profile degradation. A key finding is that velocity driven convective transport becomes dominant in the non-linear phase, overtaking conductive transport and driving the rapid collapse of core density and pressure.

Future work will extend these models toward more reactor-relevant regimes by incorporating improved physics models, enabling closer integration with experimental observations and supporting the development of robust instability control and mitigation strategies for next-generation fusion devices.

References

[1] A. Loarte et al., Nucl. Fusion 54, 033007 (2014)
[2] G.T.A. Huysmans and O. Czarny, Nucl. Fusion 47, 659 (2007); O. Czarny and G. Huysmans, JCP 227, 7423 (2008); M. Hoelzl et al., Nucl. Fusion 61, 065001 (2021)
[3] S. Futatani et al., Nucl. Fusion 54, 073008 (2014)
[4] S. Futatani et al., Nucl. Fusion 60, 026003 (2020)
[5] S. Futatani et al., Nucl. Fusion 61, 046043 (2021)
[6] Y. Suzuki, et al., Plasma Phys. Control. Fusion 63, 124009 (2021)
[7] Y. Todo et al., Plasma Fus. Res. 5, S2062 (2010)
[8] A. Civit-Bertran et al., Plasma Phys. Control. Fusion 67, 085031 (2025)
[9] Y. Todo and T. Sato, Phys. Plasmas 5, 1321 (1998)

Effective dynamics on a reduced space for plasma turbulent transport

Masanori Nunami[1,2]
[1]*National Institute for Fusion Science, Toki, Gifu 509-5292, Japan*
[2]*Nagoya University, Nagoya 464-8602, Japan*

Abstract

To construct an effective transport model, we analyze the time evolution obtained from gyrokinetic simulations of microturbulence in magnetic confinement plasmas and evaluate the structure of the reduced solution space. Solving the gyrokinetic equations yields the time evolution of the plasma phase-space distribution function, which can be interpreted as a single solution trajectory in a multidimensional parameter space. Based on gyrokinetic simulation studies, we find that representing the simulation results in a lower-dimensional space defined by the turbulence fluctuation level, the zonal flow amplitude, and the transport level integrated over wavenumber space further confines the trajectories to a reduced solution space. Focusing on the structure of this solution space, we proceed with the construction of a transport model expressed in terms of turbulence fluctuations and zonal flow amplitude, aiming to develop a model with robust extrapolation capability. Furthermore, we discuss the effects of relative "time delays" between turbulence fluctuations and zonal flow amplitude to further improve the transport model.

In magnetic fusion plasma research, understanding and predicting turbulent transport remains a critical challenge. In particular, gyrokinetic simulations, which enable accurate calculations, require enormous computational resources. Therefore, simplified transport models are strongly demanded to perform transport predictions within realistic timeframes. This study focuses on the solution trajectories obtained from gyrokinetic simulations as plasma turbulence evolves over time, and attempts to construct an effective transport model on the solution space formed by these trajectories.

In our previous work [1], we found that the solution trajectories obtained by gyrokinetic simulations remain confined within a specific region of a parameter space composed of three variables: turbulent fluctuation $\mathcal{T}$, zonal flow amplitude $\mathcal{Z}$, and transport coefficient χ. Assuming that this constrained space can be regarded as a universal space, analogous to the renormalized trajectory in quantum field theory or the inertial manifold in dissipative systems, allows us to discuss it as the solution space for plasma turbulence, eliminating the ambiguity of extrapolation. To express this confined space mathematically, we derive a minimal mathematical model by considering phenomenological requirements for an effective turbulent transport model: increase in the transport coefficient with increasing turbulent fluctuations, decrease in the transport coefficient with increasing zonal flow, finiteness of the transport coefficient in the zero limit of zonal flow, and the existence

of a combined invariant between turbulent fluctuations and zonal flow. The model is

$$\chi(t) = \mathcal{F}(\mathcal{T}(t), \mathcal{Z}(t)) = \frac{C_1 \mathcal{T}(t)^{\alpha}}{C_2 + \mathcal{Z}(t)^{\beta}/\mathcal{T}(t)}.$$

For the solution trajectory data obtained from gyrokinetic simulations, we found that the possible range of β, which represents the zonal-flow contribution in this mathematical model, can be strongly constrained by optimizing a quantity obtained by integrating the error between the mathematical model and the simulation results over the parameter space excluding β [2]. This procedure yields the range $0.5 < \beta < 0.7$, which is very close to the tentative value $\beta = 0.5$ discussed in our previous work [1].

Furthermore, we attempt to improve the model by introducing the effect of relative "time delays" in the time-series data for each variable $\mathcal{T}$, $\mathcal{Z}$, and χ. For each variable, we explicitly incorporate the time delays of $\mathcal{T}$ and $\mathcal{Z}$ from the transport coefficient into the mathematical model as $\Delta t_{\mathcal{T}}$ and $\Delta t_{\mathcal{Z}}$,

$$\chi(t) = \tilde{\mathcal{F}}(\mathcal{T}(t), \mathcal{Z}(t)) = \frac{C_1 \mathcal{T}(t - \Delta t_{\mathcal{T}})^{\alpha}}{C_2 + \mathcal{Z}(t - \Delta t_{\mathcal{Z}})^{\beta}/\mathcal{T}(t - \Delta t_{\mathcal{T}})}.$$

We then evaluate the error between the mathematical model and the simulation data in the parameter space spanned by these time delays. The results indicate that $\Delta t_{\mathcal{T}} > \Delta t_{\mathcal{Z}}$, corresponding that the model error is reduced more significantly in regions where turbulent fluctuations precede the zonal flow [3].

To further examine the causality implied by these time-series data, we evaluate "Granger causality [4]". This method is based on an autoregressive model that eliminates unnecessary lag terms using information criteria, enabling an assessment of causality in the data. The analysis reveals that the relative difference between the time lag at which turbulent fluctuations $\mathcal{T}$ most strongly enhance the transport coefficient and the time lag at which the zonal flow amplitude $\mathcal{Z}$ most strongly suppresses the transport coefficient is consistent with the region where the model error is minimized in the $\Delta t_{\mathcal{T}}$-$\Delta t_{\mathcal{Z}}$ space. In other words, data-driven causality supports a temporal sequence in which turbulent fluctuations precede zonal flow.

Finally, we plan to extend this methodology beyond the specific functional forms discussed here to more general representations, with the aim of developing a transport model with high extrapolation capability.

References

[1] K. Fujii and M. Nunami, Plasma and Fusion Research **17**, 2403030 (2022).

[2] M. Nunami, *et al.*, Plasma Phys. Control. Fusion **67** 065038 (2025).

[3] K. Fujii and M. Nunami, AAPPS-DPP (2025).

[4] C. W. J. Granger, Econometrica **37**, 424 (1969).

Development of models for time-dependent simulations of the pedestal region

E. Narita[1,2], N. Aiba[3], M. Honda[1], H. Urano[3]

[1]Graduate School of Engineering, Kyoto University, Kyoto, Japan
[2]National Institute for Fusion Science, Gifu, Japan
[3]National Institutes for Quantum Science and Technology, Ibaraki, Japan

1 Introduction

The confinement performance of H-mode plasmas largely depends on the pressure profile in the pedestal region. EPED1 model [1] is a widely used pedestal model, which determines the pedestal height and width based on MHD stabilities and turbulence without considering energy fluxes. The pressure in the pedestal region of a type-I edge localized mode (ELM) H-mode plasma gradually increases in the transport timescale, and then it suddenly decreases when it reaches the upper limit constrained by MHD instabilities and turbulence. Therefore, we need to solve transport, checking whether the pressure is lower than the upper limit at each time step. In this study, we propose an empirical transport model for the edge region, and construct a neural-network-based ideal MHD stability model. These models are introduced into a transport code and are used to perform transport simulations of H-mode plasmas with ELMs.

2 Empirical transport model for the edge region

A pedestal transport model that is widely used and reliable has not been established. One of the difficulties for the construction of pedestal transport models come from the fact that various transport channels bring transport into the region. In this study, we propose a model to predict transport coefficients using experimental observations. JT-60U experiments indicate that the ELM frequency f_{ELM} depends on the heating power, and the loss of the stored energy due to the ELM normalized by P, $f_{\mathrm{ELM}}\Delta W_{\mathrm{ELM}}/P$, is almost constant [2]. Based on the observations, we assume that f_{ELM} and $f_{\mathrm{ELM}}\Delta W_{\mathrm{ELM}}/P$ can be estimated by a given P, and predict the transport coefficients to match their values. Here, we solve a transport equation and evaluate the MHD stability at each time step. When an MHD mode is unstable, we make the pressure decrease, assuming an ELM. A similar approach has already been taken by the previous study [3, 4], where they used an empirical model depending on the heating power for the diffusivity in the inter-ELM phase, and applied an increased diffusivity based on the eigenfunction of the unstable MHD modes for the decrease in the pressure due to ELMs. In this study, the diffusivity in the inter-ELM phase and the decrease in the pressure due to ELMs are estimated based on the experimental observations.

For the sake of simplicity, we use a given density profile and a given pedestal width. A pressure limit is determined by the MHD stability analysis. Under the condition, we need to evaluate the heat diffusivity in the inter-ELM phase and the amount of the temperature reduction due to ELMs to predict the time evolution of the temperature profile. To determine these unknown

parameters to match the given $f_{\rm ELM}$ and $f_{\rm ELM}\Delta W_{\rm ELM}/P$, we introduce adjustable profiles, fac_χ and fac_T shown in figure 1. For the heat diffusivity in the inter-ELM phase, the critical gradient model [5] is used in the core region, and the diffusivity in the pedestal region is evaluated by multiplying the diffusivity given by the critical gradient model by fac_χ, which is defined by $\mathrm{fac}_\chi = f(\rho_{\rm ped})/f(\rho)$. Here, $\rho_{\rm ped}$ is the normalized minor radius location of the pedestal shoulder and $f(\rho)$ is given as a Gaussian distribution: $f(\rho) = (2\pi c_\chi^2)^{-0.5} \exp\left(-\frac{(\rho-(1+\rho_{\rm ped})/2)^2}{2c_\chi^2}\right)$. As shown in figure 1(a), the heat diffusivity in the pedestal region increases with c_χ. For the temperature reduction due to ELMs, the temperature is multiplied by fac_T, which is defined by $\mathrm{fac}_T = \left(0.5\cos\left(\frac{\pi}{1-\rho_{\rm ped-1}}(\rho-\rho_{\rm ped-1})\right)+0.5\right)c_T + (1-c_T)$. As shown in figure 1(b), the amount of the temperature reduction increases with c_T. For a given combination of c_χ and c_T, $f_{\rm ELM}$ and $\Delta W_{\rm ELM}$ can be estimated using the calculation results. Therefore, we can find the combination that fits the experimental observations by the scan of c_χ and c_T.

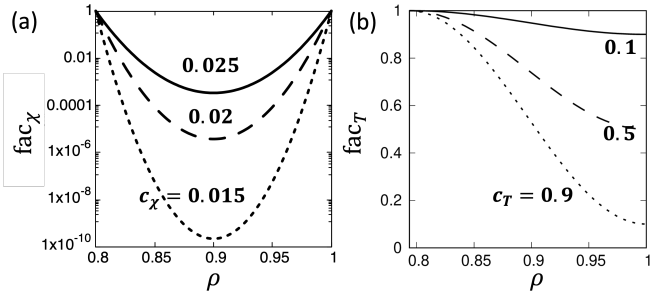

Figure 1. The radial profiles of (a) fac_χ and (b) fac_T.

3 Neural-network-based ideal MHD stability model

If the condition of the ELM occurrence is determined with an ideal MHD stability code MARG2D [6], it takes about 60 seconds. It will take an unreasonable long time for transport simulations, checking the stability at every time step. We have constructed a neural-network-based ideal MHD stability model, MARG2D-NN, which predicts stabilities of toroidal modes of $n = 1, 2, 3, 4, 5, 6, 8, 10, 15, 20, 30$. Here, n is the toroidal mode number. The inputs of MARG2D-NN are the radial profiles of the electron density, the electron and ion temperatures, the safety factor, the current, the ellipticity, and the triangularity. MARG2D-NN has been constructed by supervised learning with a fully connected neural network model. Training data were generated by MARG2D calculations with different profile combinations, and the number of the training datasets is 3,978. In the training datasets, the output of the unstable case is unity, and that of the stable case is zero. As we use the sigmoid function as the activation function in the output layer, the input case is judged to be unstable when the output is larger than 0.5. The MARG2D-NN predicts the stability in about 10^{-4} seconds, and the accuracy is higher than 95 %

4 Transport simulations of H-mode plasmas with ELMs

The empirical transport model and MARG2D-NN have been introduced into the transport code TRESS. We performed transport simulations assuming an ITER-like plasma: the major radius $R = 6.4$ m, the minor radius $a = 2.0$ m, the plasma current $I_{\rm P} = 4.7$ MA, the toroidal magnetic field $B_{\rm T} = 1.8$ T, and the electron cyclotron heating power $P = 30$ MW. We fix the density profile, the heating power profile, and the pedestal width as $\Delta_{\rm ped} = 0.1$, and use the

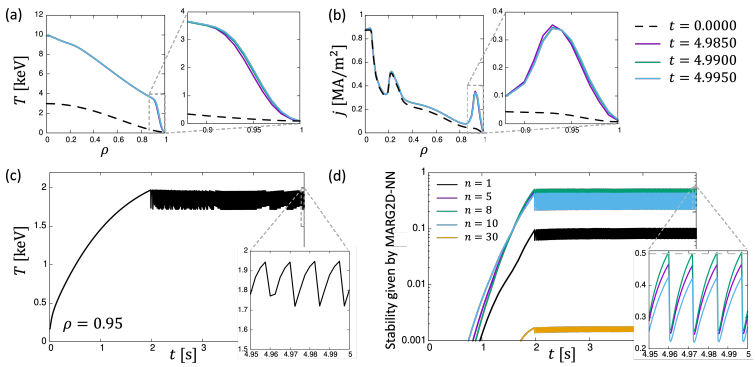

Figure 2. The radial profiles of (a) the temperature and (b) the current. The time evolution of (c) the temperature at the minor radius $\rho = 0.95$ and (d) the output of MARG2D-NN given as the stability. In the transport simulation, $c_\chi = 0.0195$ and $c_T = 0.17$ are used.

same transport model for the electrons and ions. We do not solve the magnetic equilibrium, but the change in the bootstrap current due to the change in the temperature profile is considered.

A simulation is executed with $c_\chi = 0.0195$ and $c_T = 0.17$ as shown in figure 2. In the simulation, the temperature increases from the initial profile (the broken line in figure 2(a)), and goes into the ELM phase. Due to the steep temperature gradient in the pedestal region, the bootstrap current increases as shown in figure 2(b). In the ELM phase, the temperature changes oscillatory as shown in figures 3(a) and (c). The MHD stability is analyzed by MARG2D-NN at all time steps, showing that the $n = 8$ is most unstable and determines the pedestal height as shown in figure 3(d). As the simulation takes only about 50 seconds, we can repeat it with different combinations of c_χ and c_T.

We have evaluated $f_{\rm ELM}$ and $\Delta W_{\rm ELM}$ for different combinations of c_χ and c_T as shown in figure 3. The time evolution of the temperature profile with ELMs can be obtained if the experimental conditions, $f_{\rm ELM}$ and $f_{\rm ELM}\Delta W_{\rm ELM}/P$, are given. We will develop a fast surrogate model for the magnetic equilibrium and perform transport, MHD stability, and magnetic equilibrium coupling simulations in the future.

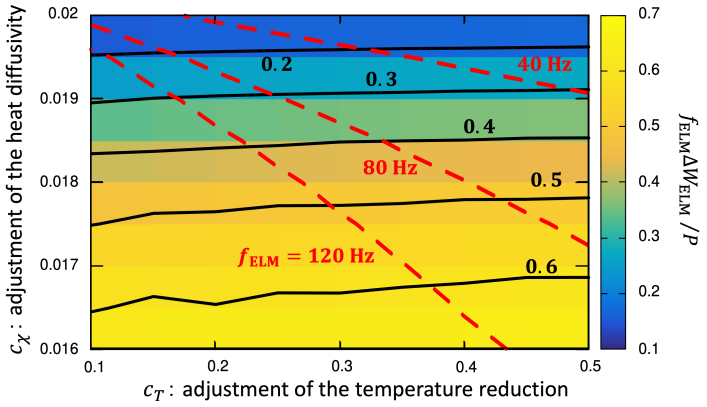

Figure 3. The dependence of $f_{\rm ELM}\Delta W_{\rm ELM}/P$ (heat map) and $f_{\rm ELM}$ (red lines) on c_χ and c_T.

References

[1] P.B. Snyder *et al.,* Phys. Plasmas **16** 056118 (2009).
[2] H. Urano *et al.,* Nucl. Fusion **53** 083003 (2013).
[3] N. Hayashi *et al.,* Nucl. Fusion **47** 682 (2007).
[4] T. Ozeki and JT-60 Team, Phys. Plasmas **14** 056114 (2007).
[5] S.C. Jardin *et al.,* J. Comput. Phys. **277** 8769 (2008).
[6] N. Aiba *et al.,* Comput. Phys. Commun. **175** 269 (2006).

Development of Impurity Transport Simulation for Detached Tokamak Plasmas in the SOL and Divertor Regions

Apiwat WISITSORASAK[1)], Naohiro Kasuya[2)],Atsushi Fukuyama[3)]

[1)]*Department of Physics, King Mongkut's University of Technology Thonburi, Bangkok, Thailand*

[2)]*Research Institute for Applied Mechanics, Kyushu University, Fukuoka, Japan*

[3)]*Department of Nuclear Engineering, Kyoto University, Kyoto, Japan*

31 January 2026

Keywords: impurity transport, scrape-off layer (SOL), tokamak, 5-point model, detachment

1 Introduction

Impurities in tokamak plasma introduce several deleterious effects on the overall performance of the devices. A large amount of impurities can dilute the fuel and reduce the rate of fusion reactions. Furthermore, one of the most immediate effects is the loss of radiated power, which leads to lower plasma temperatures.Excessive edge cooling destabilizes the plasma and leads to plasma disruption, which can severely damage the wall and other structures. On the other hand, impurity ions from the plasma-facing components, such as tungsten, can travel farther from the edge and cause significant radiation in the core. This prevents the plasma from reaching a high enough temperature for ignition [1]. Hence, the concentration of impurities should be minimized.

Despite the downside effects, the radiation of plasma impurities nevertheless has some helpful consequences. Injection of noble gases such as argon or neon is intentionally used to increase radiation in the edge region of the plasma. A well-controlled amount of these seeded impurities helps to disperse the plasma power exhaust over wider surface areas and reduce the temperature in front of the plasma-facing components. This radiative cooling is the primary mechanism for accessing the detached plasma regime, a state where plasma pressure and particle flux to the divertor targets are significantly reduced, thereby protecting the wall materials from erosion and melting.

To accurately simulate this complex interplay between impurity transport and divertor physics, we have developed a new simulation module, TASK/CSD (Core-SOL-Divertor), within the integrated transport code TASK. This module extends the previous transport models by explicitly incorporating plasma detachment physics. Volumetric recombination (particle

author's e-mail: apiwat.wis@kmutt.ac.th

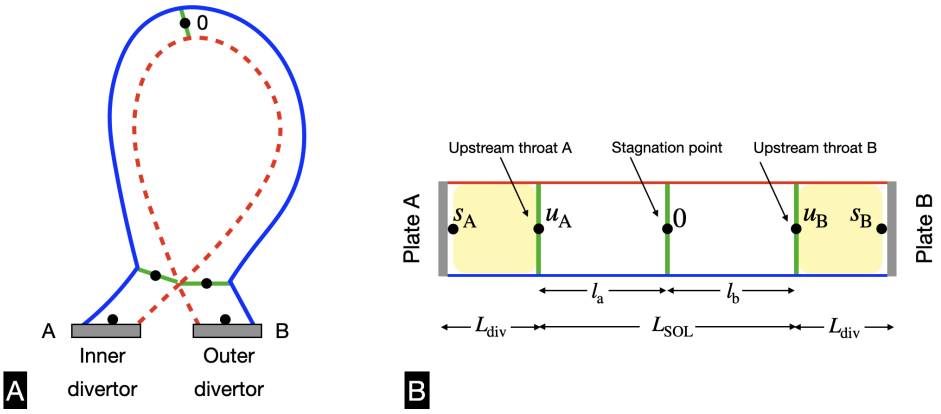

Fig. 1 Schematic diagram showing the geometry of the five-point model which considers the transport along the magnetic field.

sink) and charge-exchange friction (momentum sink) terms have been added to the fluid equations. These improvements allow the TASK/CSD code to investigate the transition from the attached to the detached state, capturing the characteristic flux rollover and temperature collapse driven by impurity radiation.

2 Methodology

To dynamically model the SOL and divertor plasma, one may reduce the complexity of the problem by considering only the transport along a magnetic field line. Instead of using a 1D or 2D transport model, one can focus on the relevant physical quantities of the plasma at specific points along the field line. The simplest model is the so-called two-point model, which considers only two points: the upstream (or stagnation point) and the target point. However, the two-point model does not account for asymmetric transport. A five-point model was originally proposed by Hayashi-san to study thermoelectric instability. It can also be used to model the dynamic response of SOL-divertor plasma during an ELM crash, which may induce thermoelectric instability and large SOL currents [2]. The model also only considers the transport of hydrogenic species without explicitly including impurities. In this work, we first describe the five-point model. The impurity transport will be solved in the background of the hydrogenic species and will be introduced later in this section.

The geometry of the five-point model is shown in Figure 1. The model considers the flux tube closest to the separatrix in single-null or double-null plasmas. The flux tube is divided into four regions. The fluid equations are integrated and reduced to a set of nonlinear algebraic equations with physical variables at the five positions.

2.1 Model Equations

The transport equations of the hydrogenic species governing the plasma dynamics in the SOL and divertor are given by:

$$
\begin{aligned}
L_{\mathrm{SOL}}\frac{\mathrm{d}n_0}{\mathrm{d}t} &= -\Gamma_{\mathrm{uB}} - \Gamma_{\mathrm{uA}} + S_0 L_{\mathrm{SOL}},\\
L_{\mathrm{div}}\frac{\mathrm{d}n_{sB}}{\mathrm{d}t} &= \Gamma_{uB} - \Gamma_{sB} + S_B L_{\mathrm{div}},\\
L_{\mathrm{div}}\frac{\mathrm{d}n_{sA}}{\mathrm{d}t} &= \Gamma_{uA} - \Gamma_{sA} + S_A L_{\mathrm{div}},\\
\frac{m_i}{2}\left(l_b + (1+R_B)L_{\mathrm{div}}\right)\frac{\mathrm{d}\Gamma_{uB}}{\mathrm{d}t} &= n_0(T_{e,0}+T_{i,0}) - n_{sB}\left(2T_{e,sB} + (1+g)T_{i,sB}\right) - P_{\mathrm{loss},B},\\
\frac{m_i}{2}\left(l_a + (1+R_A)L_{\mathrm{div}}\right)\frac{\mathrm{d}\Gamma_{uA}}{\mathrm{d}t} &= n_0(T_{e,0}+T_{i,0}) - n_{sA}\left(2T_{e,sA} + (1+g)T_{i,sA}\right) - P_{\mathrm{loss},A},\\
\frac{3}{2}\frac{\mathrm{d}n_0 T_{e0}}{\mathrm{d}t} &= -Q_{e,uB} - Q_{e,uA} - J(\phi_{uB}-\phi_{uA})\\
&\quad +(W_{e0}+W_{e,eq,0})L_{\mathrm{SOL}},\\
\frac{3}{2}\frac{\mathrm{d}n_0 T_{i0}}{\mathrm{d}t} &= -Q_{i,uB} - Q_{i,uA} + (W_{i0}+W_{i,eq,0})L_{\mathrm{SOL}},\\
\frac{3}{2}\frac{\mathrm{d}n_{sB}T_{e,sB}}{\mathrm{d}t} &= Q_{e,uB} - Q_{e,sB} - J(\phi_{uB}-\phi_{sB})\\
&\quad +(W_{e,B}+W_{e,\mathrm{eq},B})L_{\mathrm{SOL}},\\
\frac{3}{2}\frac{\mathrm{d}n_{sA}T_{e,sA}}{\mathrm{d}t} &= Q_{e,uA} - Q_{e,sA} - J(\phi_{uA}-\phi_{sA})\\
&\quad +(W_{e,A}+W_{e,\mathrm{eq},A})L_{\mathrm{SOL}},\\
\frac{3}{2}\frac{\mathrm{d}n_{sB}T_{i,sB}}{\mathrm{d}t} &= Q_{i,uB} - Q_{i,sB} + (W_{i,B}+W_{i,\mathrm{eq},B})L_{\mathrm{SOL}},\\
\frac{3}{2}\frac{\mathrm{d}n_{sA}T_{i,sA}}{\mathrm{d}t} &= Q_{i,uA} - Q_{i,sA} + (W_{i,A}+W_{i,\mathrm{eq},A})L_{\mathrm{SOL}}.
\end{aligned}
$$

The equations for the impurity species are as follows, where $j = 1, 2, 3, ..., z_{\max}$ denotes the ionization states:

$$
\begin{aligned}
L_{\mathrm{SOL}}\frac{\mathrm{d}n_{j,0}}{\mathrm{d}t} &= -\Gamma_{j,\mathrm{uB}} - \Gamma_{j,\mathrm{uA}} + L_{\mathrm{SOL}}\Big(n_{j-1,0}\alpha_{j-1,0} - n_{j,0}\alpha_{j,0}\\
&\quad +n_{j+1,0}\beta_{j+1,0} - n_{j,0}\beta_{j,0} + S_{j,0}\Big),\\
L_{\mathrm{div}}\frac{\mathrm{d}n_{j,\mathrm{sA}}}{\mathrm{d}t} &= \Gamma_{j,\mathrm{uA}} - \Gamma_{j,\mathrm{sA}} + L_{\mathrm{div}}\Big(n_{j-1,\mathrm{sA}}\alpha_{j-1,\mathrm{sA}} - n_{j,\mathrm{sA}}\alpha_{j,\mathrm{sA}}\\
&\quad +n_{j+1,\mathrm{sA}}\beta_{j+1,\mathrm{sA}} - n_{j,\mathrm{sA}}\beta_{j,\mathrm{sA}} + S_{j,\mathrm{sA}}\Big),\\
L_{\mathrm{div}}\frac{\mathrm{d}n_{j,\mathrm{sB}}}{\mathrm{d}t} &= \Gamma_{j,\mathrm{uB}} - \Gamma_{j,\mathrm{sB}} + L_{\mathrm{div}}\Big(n_{j-1,\mathrm{sB}}\alpha_{j-1,\mathrm{sB}} - n_{j,\mathrm{sB}}\alpha_{j,\mathrm{sB}}\\
&\quad +n_{j+1,\mathrm{sB}}\beta_{j+1,\mathrm{sB}} - n_{j,\mathrm{sB}}\beta_{j,\mathrm{sB}} + S_{j,\mathrm{sB}}\Big),
\end{aligned}
$$

$$\begin{aligned}
\frac{m_Z}{2}\left(l_\mathrm{b}+(R_j+1)L_\mathrm{div}\right)\frac{\mathrm{d}\Gamma_{j,\mathrm{uB}}}{\mathrm{d}t} &= n_{j,0}T_{\mathrm{H},0}-2n_{j,\mathrm{sB}}T_{\mathrm{H,SB}} \\
&\quad+\frac{m_Z}{\tau_j}\left[\frac{1}{2}n_{j,0}v_{\mathrm{H},0}+\frac{1}{2}n_{j,\mathrm{sB}}v_{\mathrm{H,sB}}+\frac{m_Z}{2}\left(l_\mathrm{b}+(R_j+1)L_\mathrm{div}\right)\Gamma_{j,\mathrm{uB}}\right] \\
&\quad+m_z\left(l_\mathrm{b}+(R_j+1)L_\mathrm{div}\right)\left(\alpha_{j-1,\mathrm{uB}}\Gamma_{j-1,\mathrm{uB}}-\alpha_{j,\mathrm{uB}}\Gamma_{j,\mathrm{uB}}\right), \\
\frac{m_Z}{2}\left(l_\mathrm{b}+(R_j+1)L_\mathrm{div}\right)\frac{\mathrm{d}\Gamma_{j,\mathrm{uA}}}{\mathrm{d}t} &= n_{j,0}T_{\mathrm{H},0}-2n_{j,\mathrm{sA}}T_{\mathrm{H,sA}} \\
&\quad+\frac{m_Z}{\tau_j}\left[\frac{1}{2}n_{j,0}v_{\mathrm{H},0}+\frac{1}{2}n_{j,\mathrm{sA}}v_{\mathrm{H,sA}}+\frac{m_Z}{2}\left(l_\mathrm{b}+(R_j+1)L_\mathrm{div}\right)\Gamma_{j,\mathrm{uA}}\right] \\
&\quad+m_z\left(l_\mathrm{b}+(R_j+1)L_\mathrm{div}\right)\left(\alpha_{j-1,\mathrm{uA}}\Gamma_{j-1,\mathrm{uA}}-\alpha_{j,\mathrm{uA}}\Gamma_{j,\mathrm{uA}}\right).
\end{aligned}$$

To simulate the impurity influx, we calculate the impurity neutral generation at the targets via physical sputtering. The neutral impurity flux $\Gamma_{0,p}$ leaving the target plate (where p denotes either target A or B) is given by:

$$\Gamma_{0,p}=\left(Y_H\Gamma_{H,p}+\sum_{j=1}^{z_\mathrm{max}}Y_j\Gamma_{j,p}\right)\sin\Theta, \tag{1}$$

where Y_H and Y_j are the sputtering yields for hydrogen and impurity ions, respectively, and Θ is the incident angle of the magnetic field line. Assuming the neutrals are emitted with a thermal velocity v_0 and decay via ionization, the neutral density profile $n_0(z)$ near the target is modeled as:

$$n_0(z)=\frac{\Gamma_{0,p}}{v_0}e^{-z/\lambda_0},\quad\text{where}\quad\lambda_0=\frac{v_0}{n_e\alpha_0}. \tag{2}$$

These equations capture the key physics required for detachment studies: the source term S explicitly includes volumetric recombination (S_rec), acting as a particle sink at low temperatures (< 1.5 eV), and the momentum loss term P_loss accounts for friction due to charge exchange (S_mom) with neutrals.

To accurately capture the physics of plasma detachment, the model explicitly incorporates a momentum loss term, , which represents the dissipation of plasma momentum due to charge-exchange (CX) friction between the plasma ions and the neutral gas in the divertor region . This term is defined as the integrated drag force over the divertor leg length, L_div , and is calculated as

$$P_{\mathrm{loss},A}=m_i n_{sA}n_{0,sA}\langle\sigma v\rangle_\mathrm{CX}c_{sA}L_\mathrm{div}, \tag{3}$$

where m_i is the ion mass, n_{sA} and $n_{0,sA}$ denote the plasma and neutral hydrogen densities at the target plate, respectively, c_{sA} is the ion sound speed, and $\langle\sigma v\rangle_\mathrm{CX}$ is the charge-exchange rate coefficient evaluated at the local target temperature. Physically, this term quantifies the momentum transfer from the accelerating plasma flow to the background neutrals, serving as the primary mechanism for decoupling the downstream plasma pressure from the upstream pressure during high-recycling and detached conditions.

2.2 Algorithm

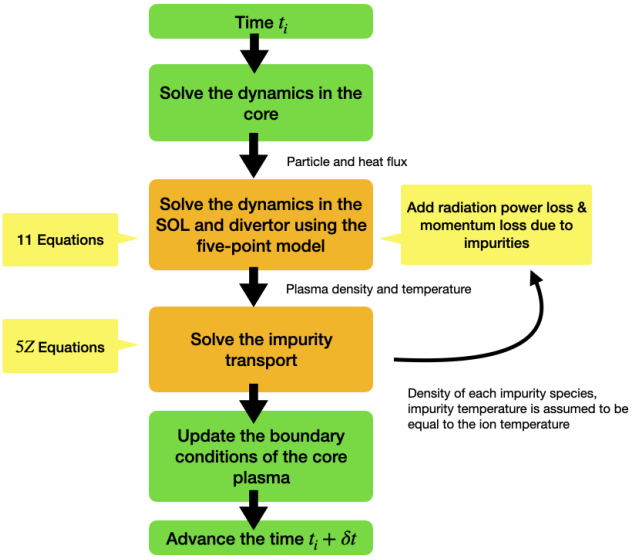

Fig. 2 Algorithm for solving the extended five-point model.

The impurity transport model can be coupled with the original five-point model to predict the densities and temperatures of both hydrogenic and impurity species. This combined model shall be named the SOL module. The SOL module can then be integrated into the main plasma simulation for the core region as follows (see Figure 2):

- At each time step, the main simulation numerically solves the plasma dynamics in the core and provides the particle and heat fluxes to the SOL module.
- In the SOL module, the original five-point model is first solved using the classical Runge-Kutta method (RK4), yielding the densities and temperatures at specific points along the field line.
- Assuming that the impurity ions share the same temperature as the main ions, the impurity transport model is then solved to determine the densities of the impurity species.
- These impurity densities are returned to the core simulation, updating the boundary conditions for the next time step.

The structure of the TASK/CSD module is designed as a hierarchical workflow centered around a main driver and a dedicated physics engine, see Figure 3. Execution begins with csd_main, which sequentially handles initialization (`csd_init`) and parameter loading (csd_parm) before entering the primary user interface, csd_menu. From this menu, the user can trigger the core solver, csd_exec, which manages the time-dependent evolution of the plasma. Within the physics kernel (csdfunc), the time loop is implemented using a 4th-order Runge-Kutta solver (RK4). This solver iteratively calls ODE_Func to evaluate the system of differential equations, relying on the ComputerFluxSource subroutine to calculate essential physical terms—such as atomic rates from OPEN-ADAS, particle sources, and momentum sinks. As shown in the data flow schematic, csd_exec functions as a state-transition operator, taking the device configuration, core fluxes, and plasma state at time t_i as inputs to compute the evolved densities and temperatures for the subsequent time step t_{i+1}.

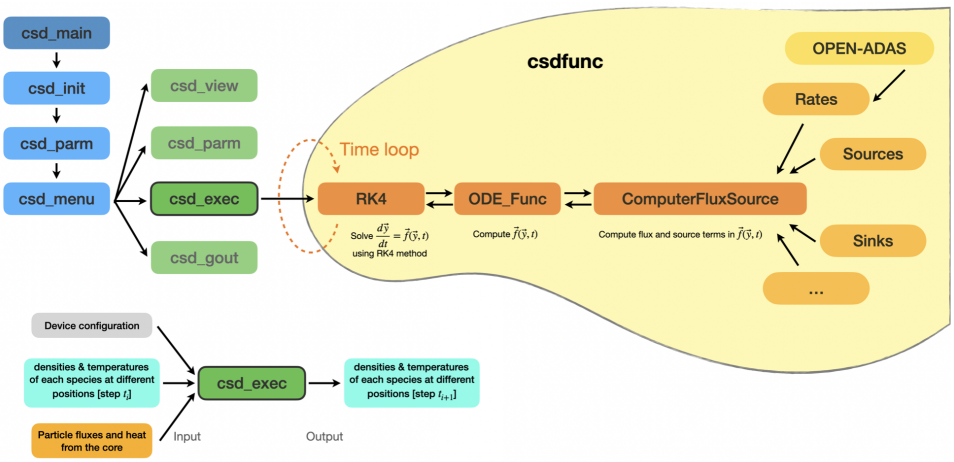

Fig. 3 Code structure and execution flow of the TASK/CSD module. The simulation is initiated by the main driver (`csd_main`), which handles parameter initialization (`csd_init`, `csd_parm`) before entering the user control interface (`csd_menu`). The core physics engine (`csd_exec`) advances the plasma state in time using a 4th-order Runge-Kutta solver (`RK4`), which iteratively calls the derivative function (`ODE_Func`) and the flux calculator (`ComputerFluxSource`) to evaluate atomic rates, source terms, and transport fluxes.

3 Results and Discussion

In this section, we present the simulation results obtained using the newly developed TASK/CSD module. To illustrate the model's capability in reproducing the transition from attached to detached divertor regimes, we employed a set of parameters representative of a medium-sized tokamak device. The simulation configuration is defined by a major radius of $R = 3.0$ m and a total separatrix surface area of $S_{\text{sep}} = 120$ m^2. The computational domain along the magnetic field line is divided into a main Scrape-Off Layer (SOL) with a connection length of $L_{\text{SOL}} = 50$ m and a divertor leg with a length of $L_{\text{div}} = 2$ m. Carbon ($Z = 6$) was selected as the impurity species to investigate the impact of radiative cooling on plasma detachment. For the initial attached conditions, the upstream electron density and temperature were initialized at $n_0 = 1.0 \times 10^{19}$ m^{-3} and $T_{e,0} = T_{i,0} = 60$ eV, respectively, with a recycling amplification factor set to 2.0.

We first examine the plasma dynamics in the sheath-limited regime, configured with an input power of $P_{\text{SOL}} = 1.5$ MW and a low recycling amplification factor to simulate a pumped divertor. As illustrated in the simulation results in Figure 4, the target particle flux (Γ_s) exhibits a linear increase proportional to the rising upstream density, with no indication of flux rollover. This linear response confirms that the plasma remains in the attached state. Consistently, the electron temperature at the divertor targets ($T_{e,s}$) stabilizes at approximately 25 eV, which is significantly higher than the 1.5 eV threshold required to trigger volumetric recombination. Regarding impurity transport, the core impurity densities demonstrate a stable linear rise, indicating continuous accumulation in the upstream region. Although the strong plasma flow generates a friction force that flushes impurities toward the targets, the impurity source term is sufficient to maintain a positive and physically consistent density profile throughout the simulation.

Subsequently, we investigated the transition to the detached plasma regime by actively controlling the heat flux and particle flux from the core. Through this systematic variation of boundary conditions, the detached plasma state was success-

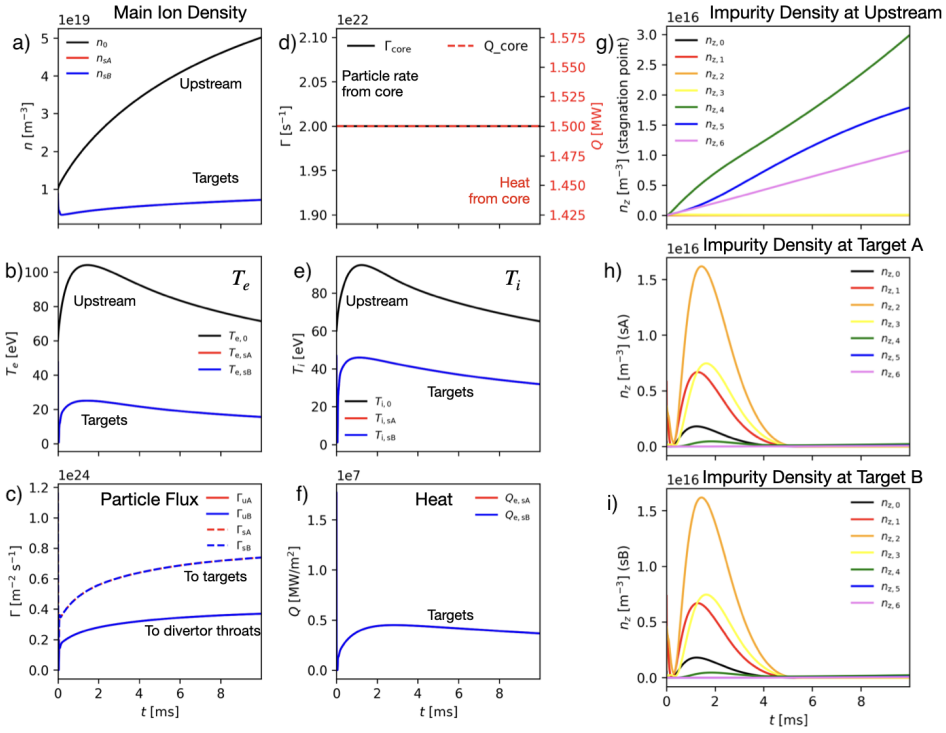

Fig. 4 Temporal evolution of SOL and divertor plasma parameters in the sheath-limited regime ($P_{\mathrm{SOL}} = 1.5$ MW). The panels illustrate: (a) the main ion densities at the upstream stagnation point (n_0) and the divertor targets (n_{sA}, n_{sB}); (b) electron and (e) ion temperatures at corresponding locations; (c) the parallel particle fluxes; (g) charge-state resolved impurity densities ($n_{z,j}$) for Carbon ($Z = 0 \ldots 6$) at the upstream interface; (h-i) impurity densities at the inner (A) and outer (B) divertor targets. The results demonstrate an attached plasma state, characterized by the linear rise of target fluxes and stable target temperatures ($T_{e,s} \approx 25$ eV) well above the recombination threshold.

fully observed. A definitive signature of detachment, the "flux rollover," is clearly evident in the simulation results, Figure 5. As the upstream density (n_0) increases, the particle flux to the targets (Γ_s) initially rises, reaches a peak, and subsequently decreases, diverging sharply from the linear behavior observed in the attached case. This rollover is driven by a precipitous collapse in the target electron temperature ($T_{e,s}$) to values below 2 eV, the threshold necessary to activate strong volumetric recombination. The simulation reveals that this recombination acts as a dominant particle sink, extinguishing over 80% of the plasma flux before it reaches the divertor plates. Furthermore, the momentum loss fraction rises to approximately 90%, confirming that charge-exchange friction has effectively decoupled the target plasma pressure from the upstream pressure. This transition is primarily initiated by radiative cooling from Carbon impurities, which lowers the divertor temperature sufficiently to trigger the recombination-dominated feedback loop.

Based on the simulation results illustrating the transition to detachment , the graphs in Figures 6 depict the non-linear response of the divertor plasma to increasing upstream density (n_0). Initially, the particle flux to the targets (Γ_s) rises linearly, characteristic of the high-recycling regime. However, as n_0 exceeds a critical threshold, the target electron temperature ($T_{e,s}$) collapses below 2 eV, triggering the onset of volumetric recombination . This cooling leads to a sharp "rollover" in the particle flux, where Γ_s decreases despite the rising upstream density. Simultaneously, the momentum and particle loss fractions increase rapidly to approximately 90% and 80%, respectively, confirming that charge-exchange friction and

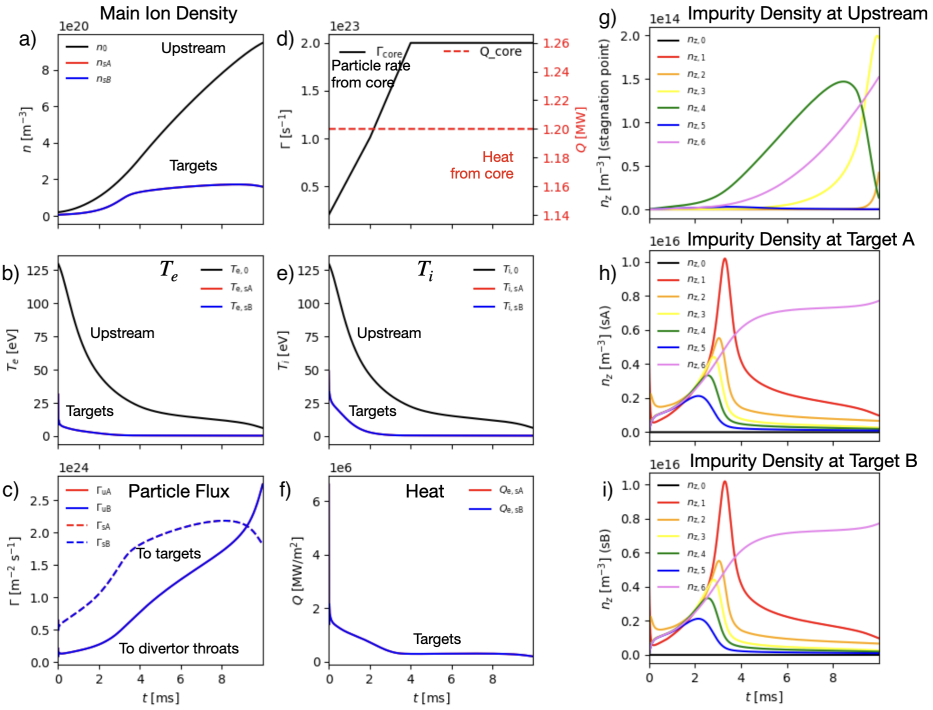

Fig. 5 Temporal evolution of SOL and divertor plasma parameters during the transition to the detached regime. The panels show: (a) the upstream main ion density (n_0) and target densities (n_{sA}, n_{sB}); (b, e) electron and ion temperatures at the upstream and target locations; (c) the parallel particle fluxes; (f) the heat fluxes; (g) carbon impurity densities at the upstream stagnation point; (h, i) impurity densities at the inner (A) and outer (B) divertor targets.

recombination have effectively decoupled the target plasma from the upstream pressure and particle sources .

4 Summary

In this study, we have developed a time-dependent Core-SOL-Divertor transport module, named TASK/CSD, designed to simulate the dynamic behavior of tokamak boundary plasmas in the presence of impurities. The model solves a comprehensive set of 11 fluid equations governing the hydrogenic plasma species, fully coupled with transport equations for impurity ions.

A key feature of this module is the explicit integration of atomic and molecular processes essential for reproducing plasma detachment. We have incorporated volumetric recombination as a particle sink and charge-exchange friction as a momentum loss mechanism. Additionally, the model accounts for impurity-induced radiative cooling, using Carbon ($Z = 6$) as a test species, which serves as the primary trigger for the temperature collapse necessary to access the detached regime.

Simulation results successfully demonstrated the validity of the model across distinct operating regimes. In the sheath-limited regime, the code exhibited stable, attached plasma conditions with target particle fluxes scaling linearly with upstream density. Furthermore, by increasing the upstream density, we successfully reproduced the transition to the detached state. Key signatures of detachment, including the characteristic particle flux rollover and a precipitous drop in target electron temperature below 2 eV, were clearly observed. These results confirm that the interplay between impurity radiation, volumetric

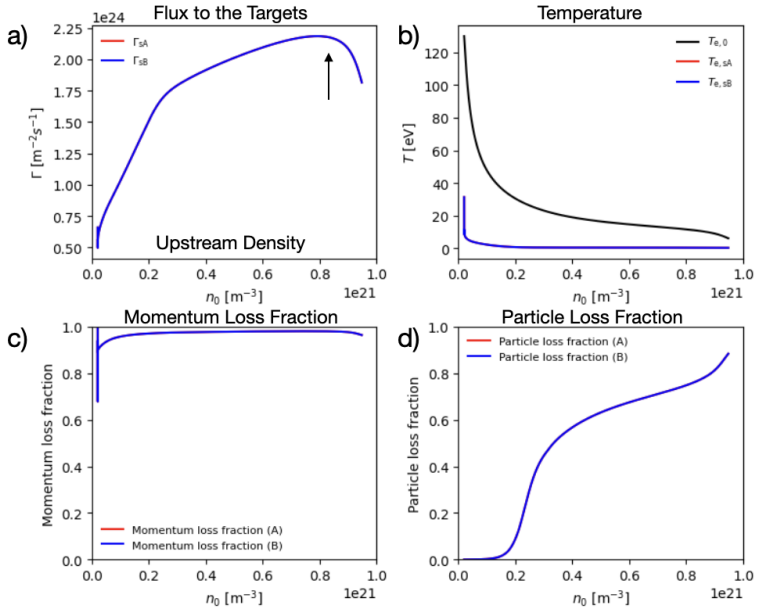

Fig. 6 Plasma parameters plotted against upstream density (n_0) during the transition to detachment. (a) The target particle flux (Γ_s) rolls over, deviating from the attached linear trend. This behavior is driven by (b) the collapse of target temperature ($T_{e,s} < 2$ eV), which triggers (d) massive volumetric recombination ($> 80\%$ particle loss) and (c) significant momentum loss ($\sim 90\%$) due to charge-exchange friction, effectively decoupling the target pressure.

recombination, and momentum loss is correctly captured by the model.

Future work will focus on the full integration of the TASK/CSD module into the comprehensive TASK transport suite to provide self-consistent boundary conditions for core plasma simulations. We also plan to validate the model and incorporate it with the TASK/SOL module to fully integrate with the solver in the core region.

Acknowledgement

This project is financially supported by the Research Institute for Applied Mechanics, Kyushu University, under the International Joint Research Program for 2025, and by the Thailand Science Research and Innovation (TSRI) Basic Research Fund for the fiscal year 2025 under project number 204518.

References

[1] P. C. Stangeby *et al.*, *The plasma boundary of magnetic fusion devices*, vol. 224. Institute of Physics Publishing Bristol, 2000.

[2] N. Hayashi, T. Takizuka, and M. Hosokawa, "Modeling of dynamic response of sol-divertor plasmas to an elm crash," *Journal of nuclear materials*, vol. 363, pp. 1044–1049, 2007.

統合コード TASK を用いた核燃焼トカマク装置不純物輸送シミュレーション

Transport simulation of impurities in nuclear fusion tokamak devices by using integrated code TASK

N. Kasuya[1,2], Y. Kawamura[2], A. Fukuyama[3], M. Yagi[4]

[1]RIAM, Kyushu University, Kasuga, Fukuoka, Japan

[2]IGSES, Kyushu University, Kasuga, Fukuoka, Japan

[3]Professor Emeritus, Kyoto University, Kyoto, Japan

[4]National Institute for Quantum and Radiological Science and Technology, Rokkasho, Aomori, Japan

E-mail: kasuya@riam.kyushu-u.ac.jp

1. Introduction

One of the most important issues for next generation tokamaks, as ITER and DEMO, is control of impurity accumulation in the core plasma. High Z impurities as tungsten used in the divertor wall are possible to cause strong radiation losses, which can degrade plasma performance. Integrated modelling simulations are useful to investigate evolution of plasma profiles, and impurity analyses of L- and H-modes for ITER have been performed using the integrated workflow [1]. For impurities, neoclassical transport plays an important role [2], so both neoclassical and turbulent transport processes must be considered. We have been developing integrated transport simulation code TASK [3,4], enabling to calculate profiles both of main plasmas and impurities in a self-consistent manner. Here we focus on this self-consistency, and impurity transport calculations are performed using TASK by considering the energy balance of nuclear burning and external heating.

2. Integrated simulation code TASK

TASK code consists of modular codes simulating equilibrium, transport, wave heating, energetic particle behavior, etc., and combination of these modules gives integrated transport analysis. In TASK code, a data exchange interface BPSD links several modules to make possible to carry out self-consistent simulations. TR module is mainly used to calculate the transport processes of the main plasma components (ions and electrons). TI module is for impurity transport, which calculates the transport processes of impurities of various charge numbers, including neoclassical, turbulent, and atomic processes. The transport coefficients for neoclassical transport are evaluated using NCLASS routine [5]. The coefficients for ionization and recombination of impurity ions are obtained from OPEN-ADAS database [6]. The code can be applied to analyze impurity transport dynamics during the formation of internal transport barriers [4]. Extension of the simulation scheme is also being carried out to introduce a surrogate model of turbulent transport [7] and a simplified core-SOL coupling model [8].

3. Particle and heat transport in burning plasmas with impurities

Core plasma impurity transport calculations were performed using the TASK code to investigate the behavior of high-Z tungsten in nuclear burning plasmas. Evaluations were carried out using the ITER device parameters. Since TASK code does not yet implement an H-mode pedestal evaluation routine, the background plasma pedestal profile is fixed for H-mode calculations here. The effect of plasma rotation [4] is also not considered. Figure 1

shows the radial profiles of main plasma components and impurities in the case with ITER baseline scenario parameters; plasma current I_p = 15MA, toroidal field B_t = 5.7 T, major radius R = 6.2 m, minor radius a = 2 m, ellipticity κ = 1.85, NBI injection power P_{NB} = 33 MW (on-axis), ECH injection power P_{EC} = 5 MW (near-axis). Calculations were performed for electrons (e), deuterium (D), tritium (T), helium (He), and impurity tungsten (W). Figure 1(e) shows no central accumulation of impurities. Figure 1(h) shows the convection velocity of impurity ions. In the pedestal region near the plasma edge, the convection velocity is negative (inward flux), but in the region closer to the center, it is positive due to the temperature screening effect, indicating no inward accumulation as same as the previous study [1]. Radiative losses are also localized near the plasma edge (Figure 1(g)).

Parameter dependencies were investigated. Increasing the heating power of ECH gives slight increase of the impurity density in the central region due to enhanced turbulent transport in this case. While it is known that ECH application can exhaust core impurities, this trend is opposite to that. Since this is a small impurity accumulation case and change in turbulent flux has a rather larger effect than change in neoclassical flux with the increased temperature gradient. A comparison was also made with and without H-mode pedestal formation. In a L-mode case the entire of plasma and impurity profiles are calculated, though in a H-mode case only the core region except the pedestal region is calculated for the background plasma. In accordance with no inward flux of impurity at the pedestal region, the impurity density at the center decreases.

These calculation results are the examples when the impurity influx from the boundary region is small, so the effect of radiation loss due to impurities on the main plasma components is small. Self-consistent behavior when the influx of the impurity affects the plasma profiles is the remaining issue. It is necessary to discuss with the formation mechanism of the H-mode pedestal.

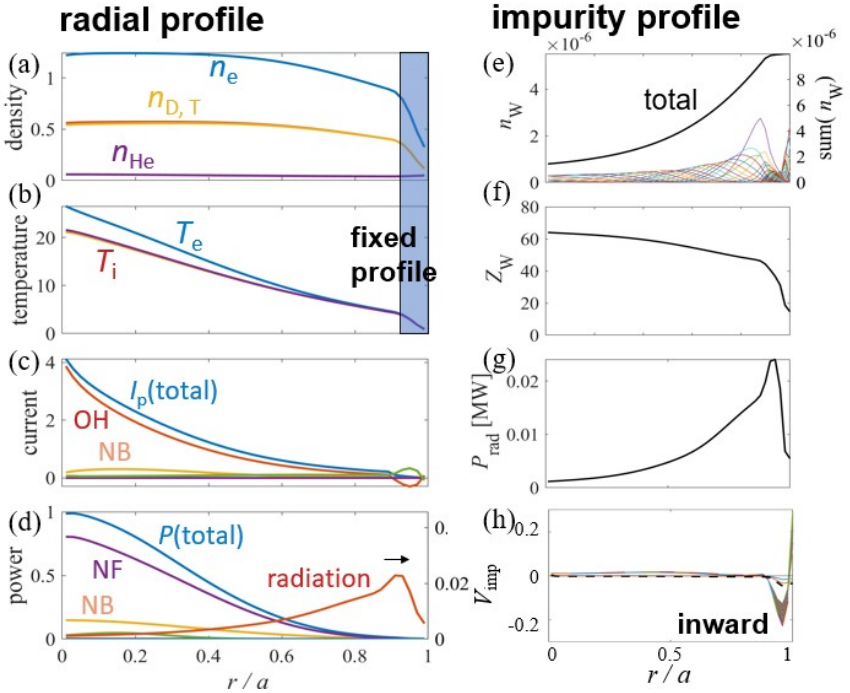

FIG. 1. Radial profiles of main plasma components and impurities with the ITER baseline scenario parameters. (a) Density, (b) temperature of the plasma main component, (c) plasma current, (d) heating and fusion power, and (e) density, (f) averaged charge, (g) radiative loss power, (h) convection velocity of the impurity tungsten are shown. The profile of the tungsten density for each valence state and their total sum are shown in (e).

Acknowledgements

This work was partially supported by the collaboration program of QST on development research of the fusion DEMO reactor, and of RIAM of Kyushu University.

References

[1] D. Fajardo, *et al.*, Plasma Phys. Control. Fusion **67**, 015020 (2025).
[2] C. Angioni, *et al.*, Nucl. Fusion **54**, 083028 (2014).
[3] M. Honda, *et al.*, Nucl. Fusion **46**, 580 (2006); http://bpsi.nucleng.kyoto-u.ac.jp/task/
[4] S. Mochinaga, *et al.*, Nuclear Fusion **64**, 066002 (2024).
[5] W. Houlberg, *et al.*, Phys. Plasmas **4**, 3230 (1997).
[6] http://open.adas.ac.uk/
[7] Y. Kawamura, *et al.*, Proc. 23rd BPSI meeting (2026) P01.
[8] A. Wisitsorasak, *et al.*, Proc. 23rd BPSI meeting (2026) 5-1.

NBCD simulation in the LHD

H. Nuga[1], R. Seki[1], K. Ogawa[1,2], H. Yamaguchi[1,2],
Y. Takemura[1,2], S. Satake[1,2], S. Kamio[3], Y. Fujiwara[4],
Y. Kawamoto[1,2], M. Yoshinuma[1], S. Sakakibara[1,2],
M. Osakabe[1,2], M. Isobe[1,2,5], M. Yokoyama[1,2],

[1]National Institute for Fusion Science, Toki, Japan
[2]The Graduate University for Advanced Studies, SOKENDAI, Toki, Japan
[3]University of California, Irvine, USA
[4]TAE Technologies, Foothill Ranch, California 92697, USA
[5]Mahasarakham University, Maha Sarakham, Thailand

Introduction The plasma stability is sensitive to the q (or ι and j) profile in the magnetic confinement fusion devices. However, in the LHD, the MSE measurement, which diagnoses the q (or ι) profile, is not always available. For this reason, most discharges in the LHD have no q (or ι) profile measurement. Although most of the poloidal magnetic field is generated by the external coil current in the LHD, the contribution of the plasma current can not be ignored, especially around the magnetic axis. Therefore, the current density profile estimation is required for the plasma stability investigation.

In addition, in the view of the fast-ion confinement study, the estimation of the current density profile has the potential to be an important criterion. The fast-ion loss mechanism is still unclear in the LHD, even in the MHD quiescent plasmas. Although the key measurement for the fast-ion confinement study is the neutron measurement, this is only available for the deuterium discharge. If the beam-driven current can be measured, it will be an important criterion of the fast-ion confinement for the hydrogen discharges because the beam-driven current is driven by fast-ions.

Unfortunately, however, it is impossible to measure only the beam-driven current. In the LHD, the plasma current is driven by the non-inductive current, j_{ni}, because there is no active external induction (such as a center solenoid). In this case, the inductive current, j_{ind}, is induced in the counter direction to cancel the non-inductive current. Although this inductive current dissipates due to the plasma resistivity, it costs ~30 seconds, which is sufficiently longer than the NB injection duration in the LHD.

Because only the net current, $j_{\mathrm{net}} = j_{\mathrm{ni}} + j_{\mathrm{ind}}$, is measurable, it is necessary to estimate both the non-inductive and the inductive currents. In this study, the neutral beam current drive (NBCD) simulation is developed for the LHD experiment analysis. This simulation is consistent with several measurements, such as n_e, T_e, T_i, and Z_{eff} profiles and the neutron measurement.

Simulation method The non-inductive current consists of three components: the bootstrap current j_{bs}, beam-driven current j_{bd}, and RF-driven current j_{rf}. In this study, the bootstrap current is calculated by DKES/PENTA, the beam-driven current is calculated by TASK3D-a and TASK/FP, and the RF-driven current is ignored.

The inductive current is governed by Faraday's Law, Ampére's Law, and Ohm's Law. In the cylindrical coordinate, the inductive electric field can be expressed as as the diffusion equation of

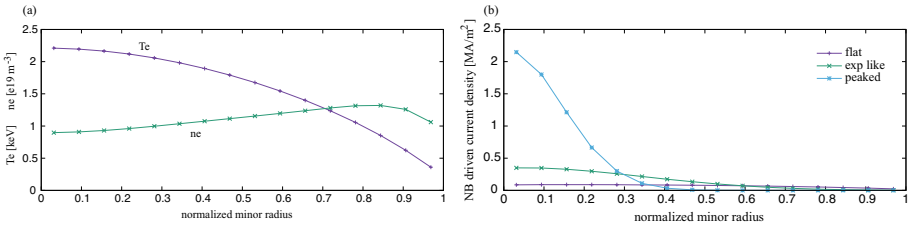

Figure 1: (a) Radial profiles of Te and ne and (b) NB birth profiles used for the validation.

the toroidal electric field.

$$\frac{1}{r}\frac{\partial}{\partial r}\left(r\frac{\partial E_z}{\partial r}\right) - \mu_0\frac{\partial}{\partial t}\sigma E_z = \mu_0\frac{\partial}{\partial t}j_{\rm ni}, \tag{1}$$

where E_z is the toroidal electric field, r is the radial position, and σ is the toroidal conductivity. The inductive current is given by $j_{\rm ind} = \sigma E_z$.

Validation by the model simulation Under the assumptions, $dl_i/dt = 0$ and $\bar{V}I_p = \int dV\boldsymbol{E}\cdot\boldsymbol{j}$, the evolution of the plasma current can be expressed as $I_p = (I_0 - I_{\rm ni})\exp(-t/(L/R)) + I_{\rm ni}$, where l_i is the normalized internal inductance, $\bar{V}$ is the loop voltage averaged over the poloidal cross-section, I_0 is the initial plasma current, $I_{\rm ni}$ is the non-inductive current, L is the plasma inductance, and R is the plasma resistivity. To validate the simulation of the electric field induction, we compared the simulation result of the net current to the above expression. Fig. 1 shows the radial profiles of Te and ne, and the NB birth profiles used for the model simulation. There are four model simulations, three non-inductive current-drive cases and one full-inductive current case, which assumes the uniform E field. The NB injection is assumed to continue for 30 s.

Table 1: Fitting parameters for the four simulation results are shown.

j prof	l_i	τ fitting	L/R
flat	0.73	3.89s	3.44s
exp like	1.5	4.09s	4.46s
peaked	3.1	4.32s	6.58s
full inductive	1.24	4.00s	4.11s

Table 1 shows the fitting parameters for the four simulation results. The value of the normalized internal inductance is at t=30s. The regression value of the time constant tau for the full inductive case is in good agreement with the L/R value. In contrast, the time constants in three non-inductive cases are separated from L/R by more than 10%. This is because the assumptions, $dl_i/dt = 0$ and $\bar{V}I_p = \int dV\boldsymbol{E}\cdot\boldsymbol{j}$, are violated for the non-inductive cases, especially immediately after NB injection starts. This result implies that the estimation of the non-inductive current in the actual LHD discharge from the regression values is invalid for the non-inductive current drive case.

Transport simulations using the integrated code TASK and a gyrofluid model

KAWAMURA Yusuke[1], KASUYA Naohiro[1,2], HONDA Mitsuru[3], FUKUYAMA Atsushi[3], YAGI Masatoshi[4]
1IGSES, Kyushu Univ., 1,2RIAM, Kyushu Univ., 3Kyoto Univ., 4QST

1. Research objective

In magnetically confined plasmas, physical processes including magnetic equilibrium, heating, and transport evolve in time and are mutually coupled. Therefore, it is effective to investigate discharge scenarios using an integrated transport code that self-consistently describes the core plasma by coupling models for individual physical phenomena. In tokamak fusion reactors, turbulence dominates heat and particle transport, and more physics-based turbulence-transport models as well as faster simulations are required. In this study, to improve the predictive accuracy of the TR transport module in the TASK code, we implemented a turbulent transport model based on gyro-fluid equations. Furthermore, to mitigate the increased computational cost, we developed a machine-learning-based surrogate model.

2. Integrated transport code TASK

TASK[1] is an integrated transport code that couples multiple modules, such as equilibrium, transport, and heating, to compute the time evolution of tokamak plasma self-consistently. The TR module evolves the density and temperature of the main plasma by solving one-dimensional transport equations such as the particle transport (1) and the heat transport (2).

$$\frac{1}{V'}\frac{\partial}{\partial t}\left(n_s V'\right) = -\frac{\partial}{\partial \rho}\left(V'\left\langle|\nabla\rho|\right\rangle n_s V_s - V'\left\langle|\nabla\rho|^2\right\rangle D_s\frac{\partial n_s}{\partial \rho}\right) + S_s \quad (1)$$

$$\frac{1}{V'^{5/3}}\frac{\partial}{\partial t}\left(\frac{3}{2}n_s T_s V'^{5/3}\right) = \frac{1}{V'}\frac{\partial}{\partial \rho}\left(V'\left\langle|\nabla\rho|\right\rangle\frac{3}{2}n_s T_s V_{Es} - V'\left\langle|\nabla\rho|^2\right\rangle n_s\chi_s\frac{\partial T_s}{\partial \rho}\right) + P_s \quad (2)$$

Here, n_s denotes the density of species s; V_s the particle pinch velocity; D_s the particle diffusivity; T_s the temperature; V_{Es} the heat pinch velocity; and χ_s the thermal diffusivity. In addition, S_s represents the particle source term, and P_s the heating (energy) source term. The NCLASS model is used for neoclassical transport, and the CDBM (Current Diffusive Ballooning Mode) model [2] has conventionally been used as a turbulent transport model. Because the CDBM model is a single-fluid model and thus cannot adequately account for mass and charge effects, introducing a more advanced physics model has remained an important challenge.

3. Gyrofluid code TGLF

The TGLF (Trapped Gyro-Landau Fluid) code [3] is a quasilinear turbulence-transport model that predicts particle, heat, and momentum fluxes driven by turbulence in tokamak plasma. In this study, we developed a coupling routine between TASK and TGLF. TGLF is executed using an input file generated by TASK. The resulting normalized fluxes, $\Gamma_s/\Gamma_{\mathrm{GB}}$ and Q_s/Q_{GB}, are converted by multiplying by the normalization factors

$$\Gamma_{GB} = n_e C_s\left(\frac{\rho_{s,unit}}{a}\right)^2, \quad Q_{GB} = n_e C_s T_e\left(\frac{\rho_{s,unit}}{a}\right)^2$$

and then dividing by the corresponding density and temperature gradients to obtain the particle diffusivity D_s and the thermal diffusivity χ_s. Here, note that TGLF normalizes its input and output variables in the CGS unit system. In addition, because the diffusivity are derived by dividing the fluxes by the corresponding gradients, the calculated diffusivity can become extremely large when the profiles are nearly flat.

Figure 1 shows the dependence of the fluxes on representative input parameters. As the normalized electron temperature gradient, a/L_{Te} (RLTS_1), increases, the electron heat flux Q_e (shown by the vermilion curve) increases markedly (Fig. 1(a)). In addition, as the temperature ratio T_i/T_e (TAUS_2) increases, the ion heat flux Q_i increases significantly (Fig. 1(b)). Thus, while some variables make a large contribution to transport, other input variables have only a negligible impact.

In TGLF, the saturation model (SAT), which determines the overall magnitude of the predicted fluxes, can be selected by choosing SAT_RULE=0–3. In Fig. 1(b), the flux obtained with SAT3 (solid line) is larger than that obtained with SAT1 (dashed line).

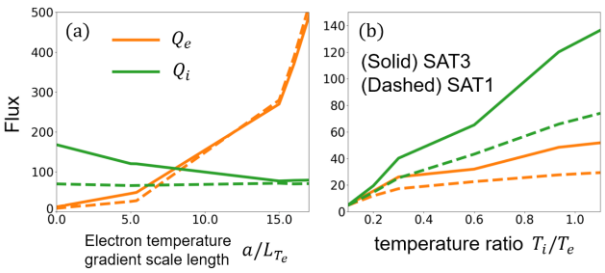

Figure 1. Dependence of the fluxes on input parameters

TGLF exhibits a strong sensitivity in that small changes in the inputs can lead to abrupt variations in the outputs. When used within an integrated transport code, the time

step must therefore be chosen sufficiently small to avoid numerical instabilities, which in turn increases the computational cost.

4. Development of a TGLF surrogate model

To improve the computational efficiency of transport calculations, we integrated an existing TGLF surrogate model (TGLF-NN) [4] into TASK. Because this model is implemented in Julia, we enabled fast execution from TASK, which is written in Fortran, by using Julia's PackageCompiler. However, because the existing surrogate model was trained based on experimental data from the DIII-D tokamak, applying ITER parameters may result in a loss of accuracy due to deviations from the training domain.

Therefore, we constructed a TGLF surrogate model targeting ITER using a neural network. The training data were generated by uniformly sampling each input variable over the full radial domain so that the samples cover the prescribed lower and upper bounds. We then readjusted the training range in the region $\rho = 0.2 - 0.8$, where ρ is the normalized radius, and performed additional training. The inputs consist of 12 variables that contribute to transport, and the outputs are four normalized flux quantities. The SiLU function was used as the activation function. We employed three hidden layers with 256 units each, and confirmed that the training was reasonable from the learning curves.

As an example of the training results, Fig. 2(a) shows the electron heat flux and Fig. 2(b) shows the ion heat flux. The vermilion curves correspond to the TGLF results, while the blue curves show the fluxes predicted by the developed TGLF surrogate model. Although some discrepancies remain, the overall trends are in good agreement.

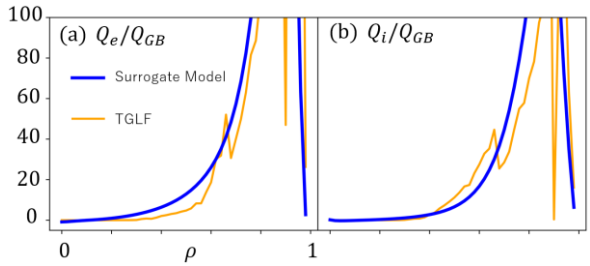

Figure 2. (a) Electron heat flux Q_e/Q_{GB} and (b) ion heat flux Q_i/Q_{GB} computed by TGLF (vermilion) and by the TGLF surrogate model (blue).

5. Simulation results

A simulation was performed for an ITER low-current, low-magnetic-field L-mode scenario [5] ($R_0 = 6.2$ m, $a = 2.0$ m, $B_0 = 2.65$ T, $I_p = 5$ MA). As heating, 20 MW of ECRF (electron cyclotron resonance heating) was applied with a Gaussian deposition profile. The particle source was also adjusted to maintain the density near the core at 0.3×10^{20} m^{-3}. Figure 3 shows the electron temperature T_e (solid black) and ion temperature T_i (dashed red) obtained using (a) the CDBM model and (b) the developed TGLF surrogate model (SAT3). Although the profile shapes differ slightly, the central temperatures are in overall agreement between the two cases and are broadly consistent with previous work [5]. Moreover, in this model, the particle diffusivity does not include the effect of an inward particle pinch. Further improvements are therefore required to accurately reproduce the core profiles.

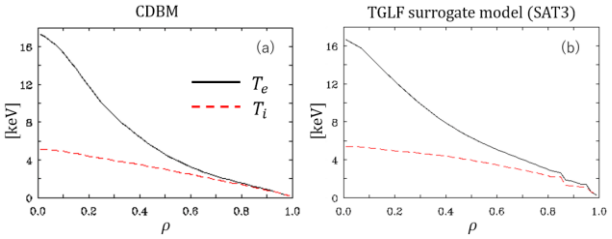

Figure 3. Electron temperature T_e(black) and ion temperature T_i(red) obtained using (a) the CDBM model and (b) the TGLF surrogate model.

6. Summary

In this study, to improve the accuracy of turbulent-transport calculations, we integrated the gyrofluid code TGLF into TASK. To address the associated computational-cost issue, we developed a neural-network surrogate model and demonstrated that it can reproduce the TGLF results with good fidelity. In the conventional CDBM model, calculations were performed assuming that electron and ion transport are identical. However, the TGLF surrogate model enables the separate evaluation of each particle. Applying this model to ITER-parameter simulations, we obtained results that are in good agreement with those from the CDBM model and with previous studies. Future work will focus on improving model accuracy by revising the training procedure, implementing particle transport, and extending the framework to impurity transport.

References

[1] https://bpsi.nucleng.kyoto-u.ac.jp/task/
[2] M. Yagi et al., Phys. Fluids B 5, 3702 (1993)
[3] J. Kinsey, et al., Phys. Plasmas 15, 055908 (2008)
[4] T. Neiser, et al., APS Division Plasma Phys. Meeting Abstracts (2022) GP11.00010
[5] D. Fajardo, et al, Plasma Phys. Control. Fusion 67, 015020 (2025)

Evaluation of the Effects of Electron Cyclotron Waves or Negative-Ion-Based Neutral Beam Injection on Tungsten Transport Characteristics in JT-60U Plasmas

TANAKA Seiya 1), FUJITA Takaaki 1), OKAMOTO Atsushi 1), KAWACHI Yuichi 1),
YASUI Kazutoshi 1), HIRAI Hajime 1), NAKANO Tomohide 2)

1) Nagoya Univ., 2) QST

1. Introduction

Tungsten (W), which will be used as the plasma-facing material in ITER, causes significant radiation loss when mixed into the core plasma; therefore, characterization of transport and accumulation is important. In JT-60U experiments, it has been reported that W accumulation in the plasma center is suppressed when Electron Cyclotron (EC) waves or Negative-ion-based Neutral Beams (N-NB) are injected in addition to Positive-ion-based Neutral Beams (P-NB) [1]. The purpose of this study is to reproduce W transport and accumulation in JT-60U using TOTAL code to quantitatively evaluate transport coefficients and W density distributions under EC or N-NB injection conditions.

2. Calculation Model in TOTAL (Toroidal Transport Analysis Linkage)

TOTAL is an integrated code capable of solving 2-D equilibrium magnetic field analysis and 1-D heat and particle transport analysis in a time-dependent manner. In the TOTAL code, the particle flux Γ_Z for tungsten ions with charge state Z is expressed by the following equation:

$$\Gamma_k = -\left(D_k{}^{\mathrm{NC}} + D_k{}^{\mathrm{AN}}\right)\frac{\partial n_k}{\partial \rho} + \left(v_k{}^{\mathrm{NC}} + v_k{}^{\mathrm{AN}}\right)n_k,$$

$$v_k{}^{\mathrm{AN}} = C \cdot \left(v_k{}^{\mathrm{PHZ}} + v_k{}^{\mathrm{Er}}\right), \qquad D_k{}^{\mathrm{AN}} = f \cdot D_k{}^{\mathrm{NC}},$$

where, ρ is the normalized minor radius, v is the pinch velocity, and D is the diffusion coefficient. The subscripts NC and AN denote neoclassical and anomalous transport, respectively. Neoclassical transport coefficients are calculated using NCLASS [2].

Anomalous diffusion of high-Z impurities is difficult to predict theoretically, so this study assumes it is proportional to neoclassical diffusion D_k^{NC}. The anomalous pinch velocity is assumed to be proportional to the PHZ pinch and Er pinch models [3]. The PHZ and Er pinches are high-Z impurity pinch effects caused by particle orbits shifting relative to the magnetic plane due to centrifugal force when toroidal rotation is significant. Specifically, in the PHZ pinch mechanism, particles move across regions with different background plasma temperatures due to orbit deviation. Since ionization and recombination coefficients depend on the electron temperature, the charge state of tungsten ions changes during a single orbit period. The resulting variation in drift velocities generates an inward pinch. On the other hand, the Er pinch is an inward pinch resulting from Coulomb collisions in an orbit deformed by potential variations along the orbit in the counter-rotating plasma.

Analysis was done on three shots from JT-60U experiments that exhibited large toroidal rotation: E49530 (P-NB injection only), E49528 (P-NB + EC injection near plasma center), and E49523 (P-NB + N-NB injection near plasma center). The experimental waveforms for each shot are shown in Fig. 1.

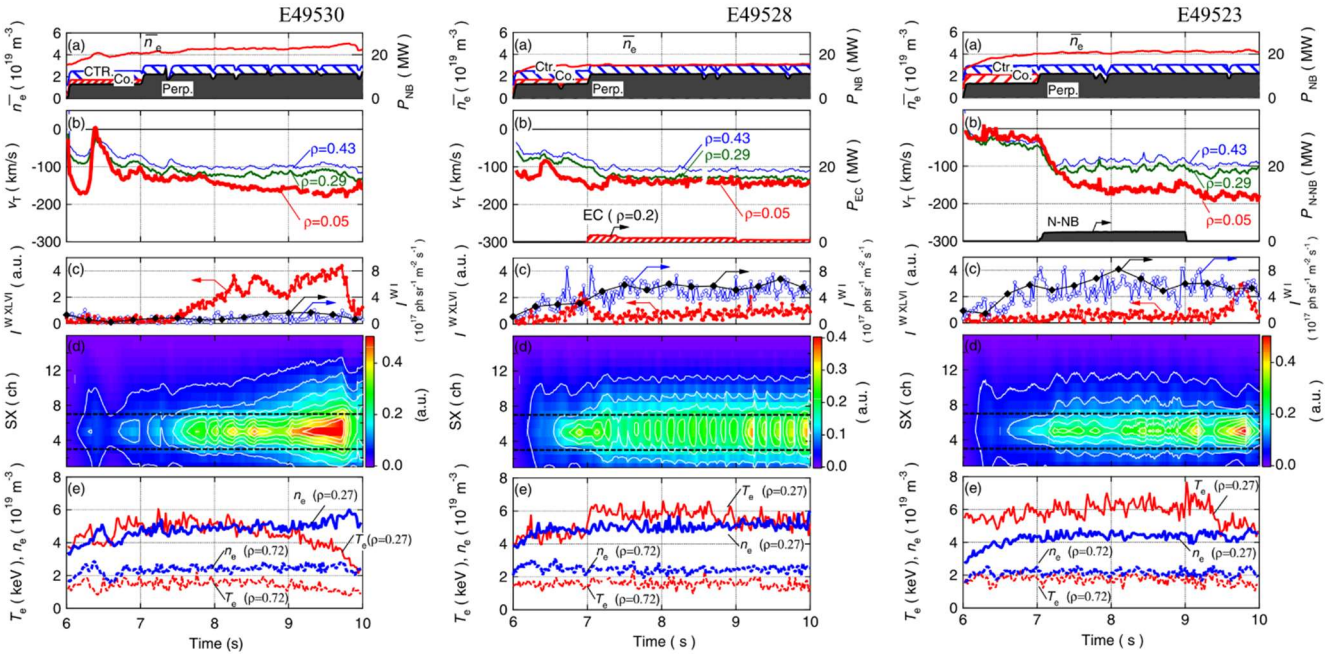

Fig. 1　Experimental waveforms for each shot [1].

In JT-60U, line-integrated SX intensity in the plasma are measured using an SX detector with 16 lines of sight (Fig. 2). The second plot from the bottom in Fig. 1 shows the contour plot of SX intensity. The vertical axis corresponds to the lines of sight in Fig. 2, with ch5 and ch6 passing through the center. As confirmed in Fig. 1, the temporal increase in soft X-rays is suppressed during EC or N-NB injection. In the TOTAL code, the experimental output is simulated by calculating the radial profile of W ion density and performing line integration of the soft X-rays [4]. In this study, we determined the transport coefficients to match the SX calculation results with the experimental results (Fig. 3).

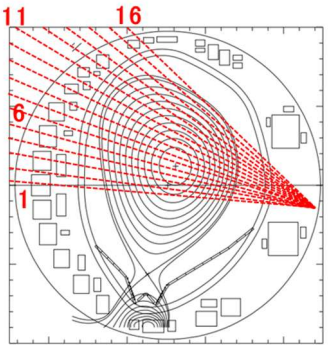

Fig. 2　SX measurement line in JT-60U

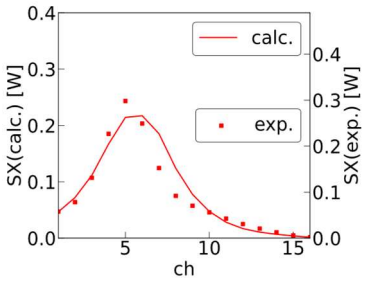

Fig. 3　Profiles of measured and calculated SX intensity (E49530, 8.0 s)

The main parameters used in the calculations are shown in Fig. 4. Experimental data corresponds to three time slices (6.1 s, 7.5 s, 9.0 s) for E49530 shot, and four time slices (6.1 s, 6.8 s, 7.5 s, 9.0 s) for E49528 and E49523 shots. The time evolution of parameters is fitted via spline interpolation.

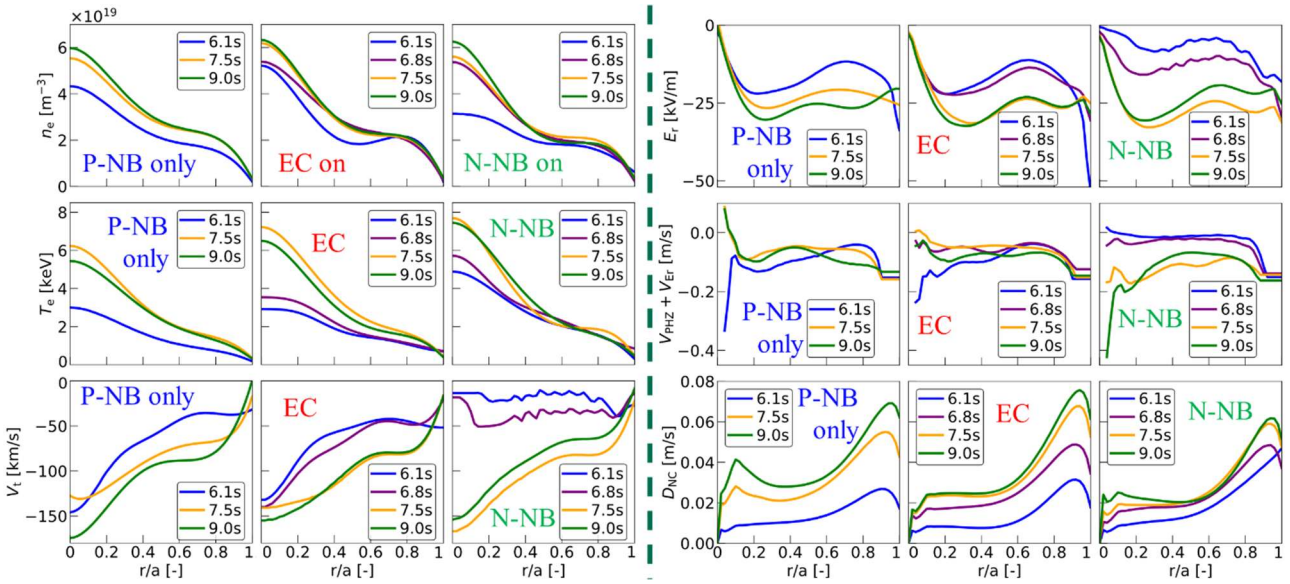

Fig. 4　The main parameters used in the calculations; electron density (n_e), electron temperature (T_e), toroidal rotation velocity (V_t), radial electric field (E_r), PHZ･Er pinch velocity ($V_{PHZ} + V_{Er}$), neoclassical diffusion coefficient (D_{NC}).

3. Results

Regarding the coefficient f for anomalous diffusion, previous research showed that experimental time evolution is roughly reproduced when $f \approx 10$; therefore, we fixed $f = 10$ in this study. Coefficients C, which relate to the anomalous pinch, were determined for each shot so that the SX profiles agreed well with the experimental data. The optimal values were found to be $C = 30$ for E49530, $C = 20$ for E49528, and $C = 10$ for E49523 as shown in Fig. 5. For the P-NB only shot, C was held constant throughout the entire duration. For the other shots, C was modified only during the change in heating method—specifically, 7.0–10.0 s for the EC shot and 7.0–9.0 s for the N-NB shot—while $C = 30$ was used for other times. Fitting calculation with experiment was performed during 6.5–9.5 s for P-NB and EC shots, and during 6.5–9.0 s for the N-NB shot. These results indicate that, under the assumption of the same f, the anomalous pinch coefficient C decreases to approximately 2/3 during EC injection and 1/3 during N-NB injection.

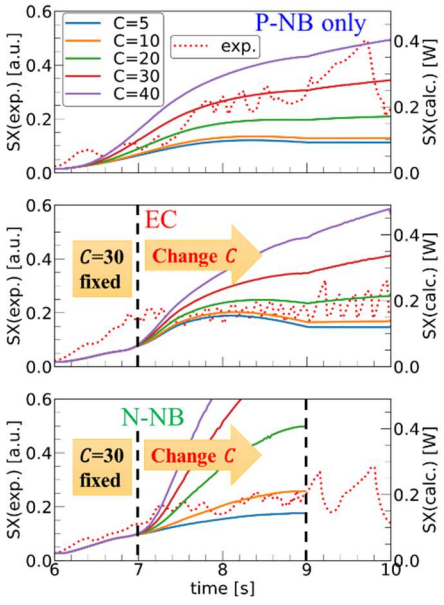

Fig. 5　SX intensity at ch 5 ($f = 10$).

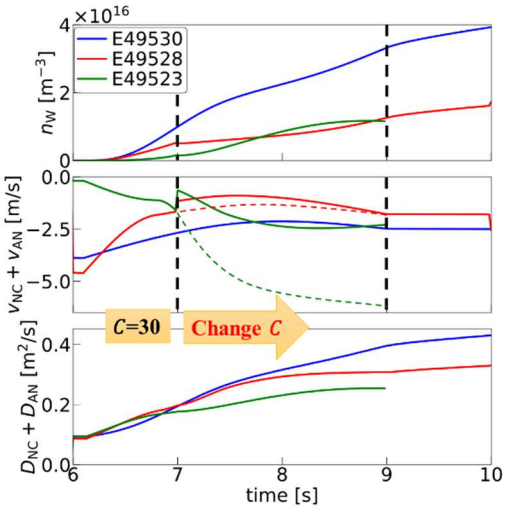

Fig. 6　Time evolution of the W density and transport coefficient near the center (average in r/a = 0 ~ 0.2).

Fig. 6 shows the time evolution of W density near the center and transport coefficients in this simulation. The dashed lines in the pinch velocity plots indicate the values when the coefficient C is fixed at 30 after 7 seconds. During EC injection (E49528), the central W density decreased significantly, while the pinch velocity was smaller and the diffusion coefficient was comparable to that in the P-NB only shot (E49530). In the N-NB injection shot (E49523), by reducing the coefficient C, the pinch velocity decreased and became to a level similar to the P-NB only shot. Although W accumulation decreased significantly in this case as well, differences in W density existed prior to 7 seconds and the diffusion coefficient became small.

Although the experimental trends after 7 seconds were reproduced, significant discrepancies were observed prior to 7 seconds. This early-stage mismatch suggests that the assumption of a constant anomalous diffusion coefficient $f = 10$ may be insufficient. Therefore, the evaluation method requires reconsideration, potentially by treating both C and f as fitting parameters, or by applying a more comprehensive transport model to better capture the transport physics in all time.

Next, Fig. 7 shows the radial distribution of W ion density for specific charge states at 8.5 seconds. The density of W ions with charge states in the 40's decreased to less than 1/3 due to EC or N-NB injection. In the N-NB injection shot, while the W density in the central region was reduced, a strong peak occurred at the center. This is considered to be the effect of the central peak of the PHZ and Er pinches at 9.0 seconds as shown in Fig. 4.

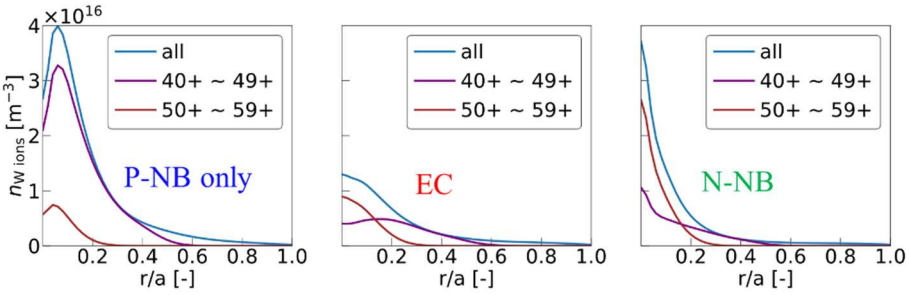

Fig. 7 Density of W ions with charge states in the 40s, 50, and all states (time = 8.5 s).

4. Summary

We reproduced the experimental results by adjusting the coefficient C related to the anomalous pinch in EC and N-NB injection shots. The TOTAL calculation results successfully demonstrated the suppression of W accumulation during EC injection. However, large discrepancies between experimental and calculated results prior to the change in heating method suggest the need to adjust the anomalous diffusion coefficient f as well as C or to apply different transport models. Future work will involve analyzing rare gas ion injection experiments to develop an anomalous transport model effective for ions with a wide range of charge states and masses, followed by verification using the TOTAL code.

Acknowledge

This research is supported by the QST Tokamak Core Plasma Joint Research Program.

References

[1] T. Nakano, et al., Nucl. Fusion **49**, 115024 (2009).
[2] W. A. Houlberg, et al., Phys. Plasmas **4**, 3230 (1997).
[3] K. Hoshino, et al., Nucl. Fusion **51**, 083027 (2011).
[4] S. Takemoto, Master Thesis, Graduate School of Engineering, Nagoya Univ. (2023).

Development of a simple analysis model for electron cyclotron current drive

Hajime HIRAI[1], Takaaki FUJITA[1], Atsushi FUKUYAMA[2], Atsushi OKAMOTO[1], Yuichi KAWACHI[1], Kazutoshi YASUI[1], Seiya TANAKA[1]

[1]Nagoya University [2]Kyoto University

1. Introduction

In a tokamak fusion reactor, the plasma current must be sustained continuously. Ohmic current drive is limited by the available magnetic flux, while it has excellent current drive efficiency. To reduce magnetic flux consumption, non-inductive current drive, such as neutral beam current drive and electron cyclotron current drive (ECCD), is required. Since electron cyclotron wave (ECW) can propagate in vacuum, antenna does not need to be placed close to the plasma, resulting in reduced antenna erosion. Furthermore, by combining multiple gyrotrons operating at different oscillation frequencies or by sweeping the injection angle using mirrors, the current-drive location can be adjusted. Owing to this high selectivity in the current drive location, various applications such as current profile control and suppression of instabilities have been actively investigated with ECCD. ECW injection conditions must be optimized based on the evolving density and temperature profile, and for analysis of long-pulsed operation, an enormous number of numerical simulations are required.

To establish a faster analysis method while maintaining sufficient accuracy, we develop a model that derives the current-drive efficiency and current-density profile avoiding the Fokker-Planck-based velocity-space analysis, which is the most time-consuming step in ECCD calculations, and instead using an alternative approach.

2. Analysis method

We use the integrated code TASK, which combines modules for analysis of equilibrium (EQ), ray tracing (WR), and kinetic transport (FP), enabling an exact analysis of ECCD. In TASK, the FP module computes the driven current based on the Fokker-Planck equation, but it is computationally expensive. To avoid full kinetic transport analysis, we develop a model based on the Fisch-Boozer formulation [1] and a theory incorporating the electron trapping effect [2]. This proposed model enables fast evaluation of the current-drive efficiency and the EC-driven current

density profile.

The current drive efficiency is given by

$$\frac{I}{P} = \frac{4{\varepsilon_0}^2 k_\mathrm{B} T_\mathrm{e}}{R n_\mathrm{e} e^3 \ln \Lambda} \cdot \frac{j^*}{p^*} \quad [\mathrm{A/W}]$$

where j^*/p^* is the normalized current drive efficiency, that is given by [1]:

$$\frac{j^*}{p^*} = \frac{3\langle wu \rangle}{5 + Z_\mathrm{eff}}$$

where $w\ (= v_\parallel / v_\mathrm{th})$ is the accelerated electron velocity parallel to the magnetic field, and $u\ (= v/v_\mathrm{th})$ is the electron speed; both are normalized by the thermal velocity.

At each ray step, the average value $\langle wu \rangle$ over all electrons on the resonance curve in the velocity space is evaluated as the weighted average of wu with the relativistic Maxwell distribution $f_\mathrm{MJ}(\gamma)$ [3] over the range of Lorentz factors that satisfy the relativistic resonance condition.

The radial profile of the driven current is derived by multiplying the current drive efficiency by the absorbed power at each ray step calculated by TASK/WR.

3. Results

Analysis was performed using the plasma parameters of JA-DEMO. The injection conditions are $P_\mathrm{EC} = 1\ \mathrm{MW}$, $f_\mathrm{inj} = 220$ GHz and $\theta_\mathrm{pol} = 0$ deg., with different injection toroidal angles θ_tor, where P_EC is the injection power, f_inj is the wave frequency, θ_pol is the injection poloidal angle. The current-drive efficiency $\eta\ (= I/P)$ and the absorbed power along the wave propagation path are shown in figure 1. The dashed line on the left indicates the point at which the fundamental resonance condition begins to be satisfied in the developed model, whereas the dashed lines on the right indicate the termination of the calculation due to sufficient ECW absorption. Resonance occurs at the up-shifted second harmonic (left peak of the absorbed power distribution) and the down-shifted fundamental (right peak). The developed model performs calculations only when the fundamental resonance is present, and the fundamental resonance ranges (enclosed by the dashed lines) approximately coincide with the widths of the current-drive efficiency and the absorbed power peaks. Note that the right-hand tail of the absorbed power distribution remains a finite value up to the right dashed lines, and that the maximum ray step varies with the injection

conditions because they determine the length of the wave propagation path.

The total driven current I_{total} is obtained by applying trapezoidal integration to the driven-current at each ray step, as summarized in table 1. The driven-current profiles for various θ_{tor} are shown in figure 2.

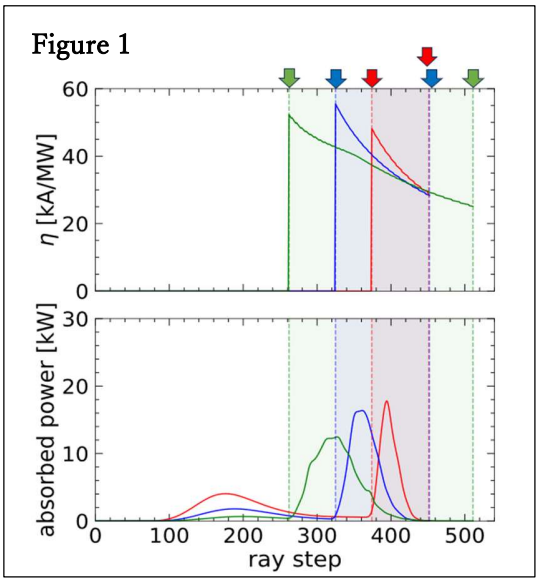

Table 1
injection power: **1 MW**
frequency: **220 GHz**
poloidal angle θ_{pol}: **0°**

θ_{tor}	I_{total}
30°	20.0 kA
35°	33.6 kA
40°	39.5 kA

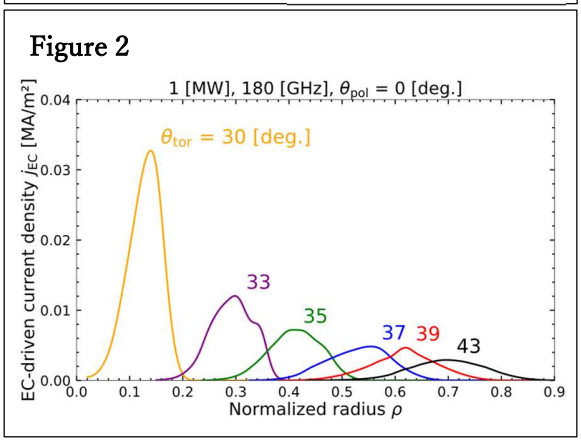

Figure 1. The current-drive efficiency η calculated with the developed model (upper figure). The current-drive efficiency is evaluated only at ray steps where the resonance condition is satisfied and the absorbed power remains finite. The absorbed power calculated by TASK/WR (lower figure) is shown for the same ray steps, which are equally spaced along the wave propagation path. The dashed lines indicated by the arrows denote the range where η is defined, and this range is projected onto the absorbed power distribution.

Table 1. Total driven current I_{total} at each toroidal angle θ_{tor}.

Figure 2. Radial profiles of EC-driven current density j_{EC} for different toroidal angles θ_{tor}.

4. Summary and Prospects

A fast current profile calculation module was developed using the Fisch-Boozer formulation, and reasonable results were obtained for current-drive efficiency. The second harmonic absorption and the finite Lamor radius effect must be considered. To verify the accuracy, the following three direct comparisons are desirable: (i) an exact solution of Fokker-Planck equation

(ii) an approximate solution (adjoint method) (iii) the EC simple analysis model in this study.

5 . Reference

[1] N. J. Fisch and A. H. Boozer, Physical Review Letters **45**, 720 (1980).

[2] G. Giruzzi, Nuclear fusion **27**, 1934 (1987)

[3] Gilberto J. Damião and Clóves G. Rodrigues, Revista Brasileira de Ensino de Física **44**, e20210271 (2022)

Effect of resonance surface position on flattening process of the density profile in reduced MHD simulation of tokamaks

Kosuke SAKAMOTO[1], Naohiro KASUYA[1,2], Masatoshi YAGI[3]
IGSES Kyushu Univ.[1], RIAM Kyushu Univ.[2], QST[3]

1. Research background and objectives

In fusion tokamak plasmas, various instabilities are excited by the presence of density and temperature gradients[1]. In addition, electromagnetic instabilities can be driven at resonant surfaces, leading to the formation of magnetic island structures. The growth and saturation of these instabilities, as well as the resulting formation of plasma profiles, play a key role in particle and heat transport in fusion plasmas, making it essential to evaluate their impact. In this study, global simulations from the core to the edge of a tokamak plasma are performed using a six-field reduced magnetohydrodynamic (MHD) model. By varying the relative positions of the temperature gradient region, where micro instabilities are excited, and the resonant surfaces, where electromagnetic instabilities are driven, the interaction mechanisms between these two types of instabilities are investigated.

2. Simulation model

In the global reduced magnetohydrodynamic code R6F [2], the time evolution of six fields—namely the electrostatic potential ϕ, vector potential A, parallel flow velocity v, density N, electron temperature T_e, and ion temperature T_i—is solved three-dimensionally in space by employing the following set of equations: (1) the vorticity equation, (2) Ohm's law, (3) the ion parallel momentum equation, (4) the continuity equation, and the evolution equations for (5) the electron and (6) ion temperatures. Here, $\varepsilon = a/R_0$is the inverse aspect ratio, $R_0$is the major radius, and $v_A = B/\sqrt{4\pi n m_i}$denotes the Alfvén velocity.

$$\frac{\partial}{\partial t}\nabla_\perp^2 F + [F, \nabla_\perp^2 F] - \delta\nabla_\perp \cdot [P_i, \nabla_\perp F] = -\nabla_\parallel^{(0)} J + [A, J] - [\Omega, P] + \mu_\perp^i \nabla_\perp^4 F - \frac{q}{\varepsilon}\mu_i \frac{1}{r}\frac{\partial}{\partial r}(rU_i) - \frac{q}{\varepsilon}\frac{m_e}{m_i}\mu_e \frac{1}{r}\frac{\partial}{\partial r}(rU_e) \tag{1}$$

$$\frac{\partial}{\partial t}\left(A - \delta^2 \frac{m_\mathrm{e}}{m_\mathrm{i}} J\right) = -\nabla_\parallel^{(0)}(\phi - \delta P_\mathrm{e}) + [A, \phi] - \delta[A, P_\mathrm{e}] + \delta^2 \frac{m_\mathrm{e}}{m_\mathrm{i}}[\phi, J] + \eta_\parallel J - 4\mu_\perp^\mathrm{e}\delta^2 \frac{m_\mathrm{e}}{m_\mathrm{i}}\nabla_\perp^2 J + \delta \frac{m_\mathrm{e}}{m_\mathrm{i}}\mu_\mathrm{e} U_\mathrm{e} + \alpha_T \delta \nabla_\parallel T_\mathrm{e} \tag{2}$$

$$\frac{\partial v}{\partial t} + [\phi, v] = -\nabla_\parallel^{(0)} P + [A, P] + 4\mu_\perp^\mathrm{i}\nabla_\perp^2 v - \mu_\mathrm{i} U_\mathrm{i} - \frac{m_\mathrm{e}}{m_\mathrm{i}}\mu_\mathrm{e} U_\mathrm{e} \tag{3}$$

$$\frac{dN}{dt} + \beta\frac{dP}{dt} = \beta[\Omega, \phi - \delta P_\mathrm{e}] - \beta\nabla_\parallel^{(0)}(v + \delta J) + \beta[A, v] + \beta[A, J] + \eta_\perp \beta \nabla_\perp^2 p - \beta\delta \frac{m_\mathrm{e}}{m_\mathrm{i}}\frac{q}{\varepsilon}\mu_\mathrm{e}\frac{1}{r}\frac{\partial}{\partial r}(rU_\mathrm{e}) \tag{4}$$

$$\frac{3}{2}\frac{dT_{\mathrm{e}}}{dt}-\frac{\beta_{\mathrm{e}}}{\beta}\frac{dn}{dt}=-\alpha_{\mathrm{T}}\delta\beta_{\mathrm{e}}\nabla_{\parallel}J+\varepsilon^{2}\chi_{\mathrm{e}\parallel}\nabla_{\parallel}^{2}T_{\mathrm{e}}+\chi_{\mathrm{e}\perp}\nabla_{\perp}^{2}T_{\mathrm{e}}-\frac{5}{2}\delta\beta_{\mathrm{e}}[\Omega,T_{\mathrm{e}}] \tag{5}$$

$$\frac{3}{2}\frac{dT_{\mathrm{i}}}{dt}-\frac{\beta_{\mathrm{i}}}{\beta}\frac{dN}{dt}=\varepsilon^{2}\chi_{\mathrm{i}\parallel}\nabla_{\parallel}^{2}T_{\mathrm{i}}+\chi_{\mathrm{i}\perp}\nabla_{\perp}^{2}T_{\mathrm{i}}+\frac{5}{2}\delta\beta_{\mathrm{i}}[\Omega,T_{\mathrm{i}}] \tag{6}$$

Here, $F:=\phi+\delta P_i$, $P_e=(\beta_e/\beta)N+T_e$, $P_i=(\beta_i/\beta)N+T_i$, $P=P_i+P_e$. The convective time derivative is defined as $d_t:=\partial_t+[\Phi,]$, and the parallel gradient operator as $\nabla_{\parallel}=\nabla_{\parallel}^{(0)}-[A,]$. Length is normalized by the minor radius a, and time is normalized by the poloidal Alfvén time $a/(\varepsilon v_A)$. The computational parameters used in this study are as follows: the major radius $R_0=1.5\,\mathrm{m}$, the minor radius $a=0.5\,\mathrm{m}$, the inverse aspect ratio $\varepsilon=0.33$, the ion skin depth $\delta=10^{-2}$, the mass ratio $m_e/m_i=1/1836$, the resistivities $\eta_{\perp}$and $\eta_{\parallel}=10^{-5}$, the thermal diffusivities $\chi_{e\perp}=10^{-5}$and $\chi_{e\parallel}=1$, the neoclassical viscosity coefficients $\mu_i=4.6\times10^{-5}$and $\mu_e=1.4\times10^{-3}$, and the thermodiffusion coefficient $\alpha_T=0.71$.The initial density profile is given by $N_{\mathrm{EQ}}=(\beta/\varepsilon)(1-r^2)^2$. The initial electron and ion temperature profiles are assumed to have the same hyperbolic-tangent functional form, with normalization factors of $\beta_e/\varepsilon$and β_i/ε, respectively.

3. Analysis results

Time evolutions were calculated starting from the initial density and temperature profiles shown in Figs. 1 and 2, under the safety factor profile (q profile, representing the magnetic field line twist) shown in Fig. 1. In this configuration, the rational surface with $q=2$ is located at $r=0.6$. As illustrated in Fig. 2, three cases were considered, in which the position of the steepest ion temperature gradient $r=r_s$was set to (i) 0.4, (ii) 0.5, and (iii) 0.8. The purpose of this setup is to evaluate the effect of varying the distance between the $q=2$rational surface and the steep temperature-gradient region. The ion and electron beta values, which determine the strength of the temperature gradients, were fixed at $\beta_i=\beta_e=0.004$, and the magnitude of the temperature gradient itself was kept identical among cases (i)–(iii). Fig 3 shows the time evolution of the internal energy for each Fourier mode in the three cases. Here, $m$and $n$denote the poloidal and toroidal mode numbers, respectively. In all cases, unstable modes initially grow during the linear phase, followed by a transition to a nonlinear phase in which interactions among different wavenumber components become dominant, and eventually reach saturation. In the nonlinear phase, low-mode-number components such as $(m,n)=(-2,1)$and $(-3,2)$dominate and form magnetic island structures in all cases. We first compare the growth characteristics in the linear phase. In cases (ii) and (iii), the linear phase (up to $t=2100$ and $t=480$, respectively) is dominated by the ion temperature gradient (ITG) instability. The ITG instability is a microscale (high-wavenumber) instability driven by steep ion temperature gradients; the resulting turbulence enhances heat transport and ultimately weakens its own drive by flattening the temperature gradient. Consistent with this picture, high-wavenumber ITG modes with resonant surfaces located near the steep temperature-gradient region grow dominantly, such as $(m,n)=(-20,11)$and $(-19,11)$in case (ii), and $(m,n)=(-24,9)$and $(-25,9)$in case (iii).In contrast, during the linear phase of case (i) (up to $t=1900$), the growth of a low-wavenumber

resonant macroscale instability, $(m,n) = (-3,2)$, dominates rather than the ITG instability. This is attributed to the placement of the temperature gradient in a region of low magnetic shear, which weakens the ITG drive. We next examine the nonlinear growth processes in each case. In cases (ii) and (iii), the ITG instability nonlinearly enhances macroscale instabilities such as the $(m,n) = (-2,1)$mode. In case (i), although the growth of the $(-2,1)$mode and ITG instability is delayed until the nonlinear phase ($t \gtrsim 2100$), similar nonlinear interactions are observed in this case as well. Furthermore, in case (ii), a rapid increase in density fluctuations is observed in the time interval $t = 3900$–4000, as shown in Fig. 4. This abrupt increase is associated with modifications of the density profile caused by a magnetic island formed around $r = 0.6$. Figs. 5 and 6 show that magnetic islands flatten the density and temperature gradients within the island while simultaneously steepening them externally. It has been determined that the steepened density gradient acts as a driving factor that excites instability, leading to the observed rapid increase in fluctuations.

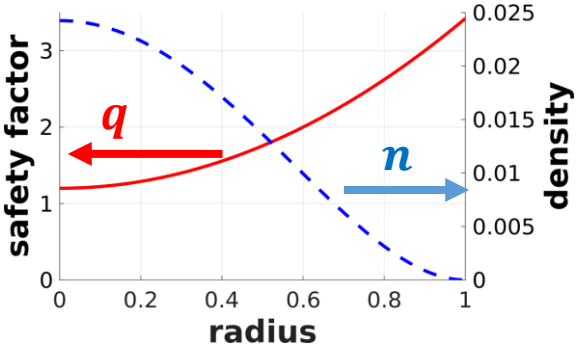

Fig. 1 Initial density profile and safety factor.

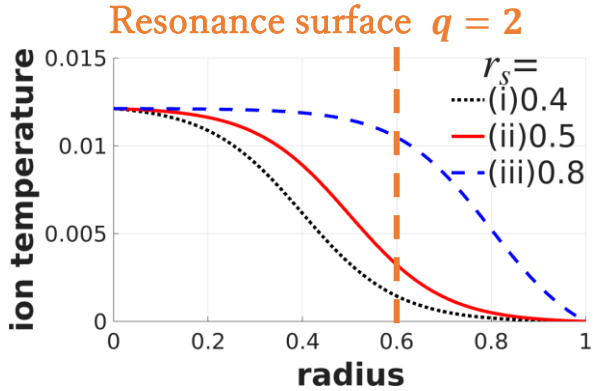

Fig. 2 Initial ion temperature profile.

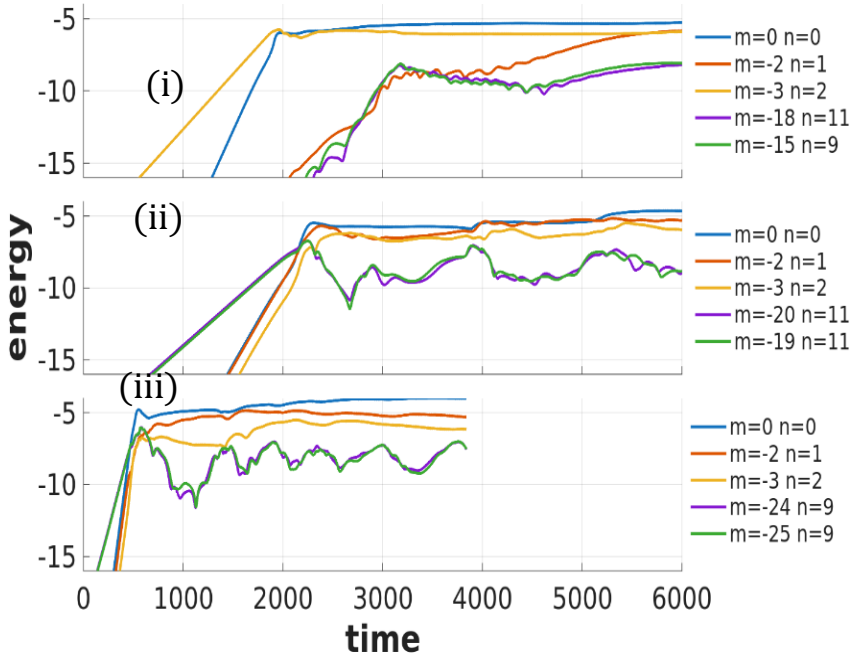

Fig. 3 Time evolution of the density fluctuation energy.
From top to bottom: cases (i), (ii), and (iii).

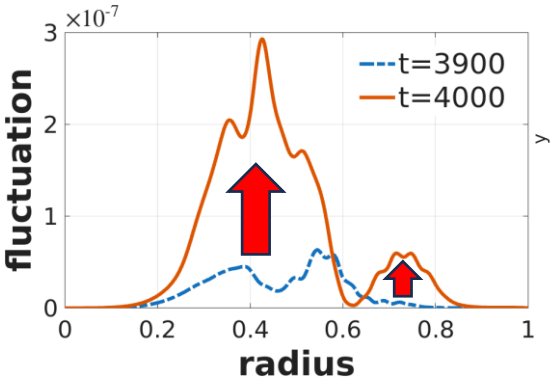

Fig 4. Radial profiles of density fluctuations at $t = 3900$ and 4000.

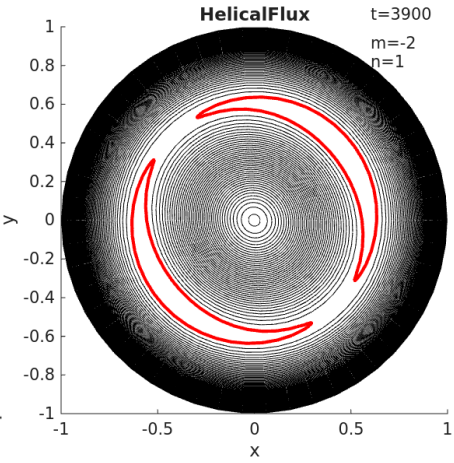

Fig5. Poloidal cross-section of the helical flux at $t = 3900$(For the condition r_s= (ii) 0.5).

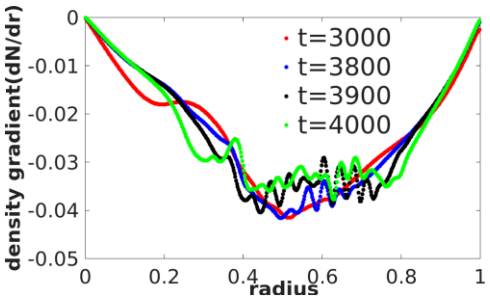

Fig 6. Radial distribution of density gradient. Red dots indicate $t = 3000$, blue dots indicate $t = 3800$, black dots indicate $t = 3900$, and green dots indicate $t = 4000$.

4. Conclusion

Using a six-field reduced MHD model, global tokamak simulations were conducted to investigate instability interactions as a function of the steep temperature gradient location. In the nonlinear regime, the ITG instability consistently enhanced the growth of the macroscopic $(-2, 1)$ mode. Furthermore, the subsequent increase in instability levels was found to be linked to density profile modifications induced by magnetic island formation, providing insight into global energy transfer among modes.

5. Acknowledgments

This work was partially supported by the collaboration program of QST on development research of the fusion DEMO reactor, and of RIAM in Kyushu University. Simulations were carried out using the supercomputer system at Computational Simulation Centre of International Fusion Energy Research Centre (IFERC-CSC) in QST.

References

[1] R. Okazaki, 核融合炉設計入門.

[2] M. Yagi, et al., Proc. 20th BPSI meeting (2023) 1-10.

A Comparative Study on Determining Methods for Multi-Variable PID Control Gains of JA DEMO Using TOTAL
TOTAL を用いた原型炉多変数 PID 制御ゲインの決定手法の比較

*Kazutoshi Yasui, Takaaki Fujita, Atsushi Okamoto, Yuichi Kawachi, Seiya Tanaka, Hajime Hirai

Nagoya Univ.

1 Introduction

The design of fusion DEMO reactors is progressing, and control of core plasma is one of the significant challenges[1]. In the reactor, numerous physical quantities are interrelated. A single manipulated variable affects many controlled variables. For example, heating inputs (NBI, ECRH, etc.) simultaneously affect not only plasma temperature rise but also current distribution. Therefore, constructing multi-variable control logic for such complex system is necessary.

Also, real-time simulation based on measured data is required for the prediction of physical quantities that are difficult to measure. This requires the development of integrated codes that simulate the core plasma. The integrated code TOTAL[3] we use is a 1.5D equilibrium and transport code that performs 1D particle and thermal transport analysis and 2D magnetic equilibrium analysis. TOTAL has the advantage of relatively low computational cost, making it suitable for real-time simulation, and it also has the multivariable feedback control function.

In TOTAL, PID (Proportional-Integral-Derivative) control is employed to control plasma parameters. The control equations are describes as follows:

$$X_j(t) = X_j^{\mathrm{pre}}(t) + X_j^{\mathrm{base}}(t) + \sum_k C_j^k(t) \tag{1}$$

$$C_j^k(t) = G_{\mathrm{p},j}^k \Big(e_k(t) + \frac{1}{\tau_{\mathrm{i},j}^k} \int e_k(t')dt' + \tau_{\mathrm{d},j}^k \frac{de_k(t)}{dt} \Big) \tag{2}$$

$$e_k(t) = Y_k^{\mathrm{targert}} - Y_k(t) \tag{3}$$

Here, X_j is the j-th manipulated variable, X_j^{pre} is the pre-programmed value, X_j^{base} is the base (steady-state) value, C_j^k is the correction value of the j-th manipulated variable determined by the k-th controlled variable, $G_{\mathrm{p},j}^k$ is the proportional control gain for controlling the k-th controlled variable with the j-th manipulated variable, $\tau_{\mathrm{i},j}^k$ is the integral time constant, $\tau_{\mathrm{d},j}^k$ is the derivative time constant, $e_k(t)$ is the deviation of the k-th controlled variable, Y_k^{target} is the target value of the k-th controlled variable, and Y_k is the k-th controlled variable.

Conventionally, the constants $G_{\mathrm{p},j}^k$, $\tau_{\mathrm{i},j}^k$, and $\tau_{\mathrm{d},j}^k$ required for these calculations have been determined by rules of thumb. In this study, we examined multivariable PID control gains and time constants using the step response characteristics of the controlled variables, aiming to construct appropriate multivariable control logic for JA-DEMO[2] reactor plasma.

In this study, we set line-average electron density $\bar{n}_{\mathrm{e}}$ and fusion power P_{fus} for the controlled variables, and NB power P_{NB} and pellet fueling rate f_{pel} for the manipulated variables.

2 Determination of multi-variable control gains and control tests

We attempted to determine the multi-variable PID control gains and time constants using step response characteristics of the controlled variables. The procedure to obtain step response of the controlled variables is as follows:

i. Turn off feedback control at the time when each parameter has stabilized ($t = 250$ s).
ii. At $t = 260$ s, change each manipulated variable by $\pm 10\%$.

The responses of the controlled variables are shown in figure 1.

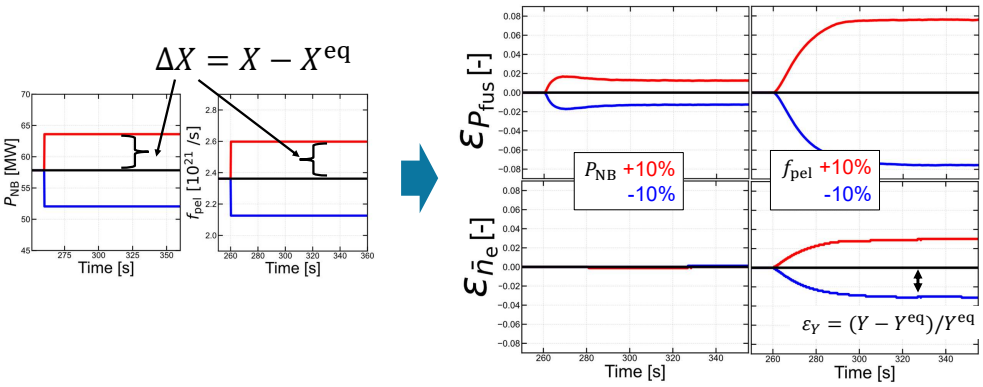

Figure 1: The responses of each controlled variables.

2.1 Determining method 1

For the first method to determine the gain, we expressesed the response of the controlled variable as a matrix and determines the gain from it. To calculate the gain, first calculate the response matrix $\boldsymbol{A}$. $\boldsymbol{A}$ is calculated as follows:

$$\begin{pmatrix} \varepsilon_{P_{\mathrm{fus}}} \\ \varepsilon_{\bar{n}_{\mathrm{e}}} \end{pmatrix} = \boldsymbol{A} \begin{pmatrix} \Delta P_{\mathrm{NB}}/P_{\mathrm{NB}}^{\mathrm{eq}} \\ \Delta f_{\mathrm{pel}}/f_{\mathrm{pel}}^{\mathrm{eq}} \end{pmatrix} \tag{4}$$

Here, each variables are defined as follows:

$$\varepsilon_{P_{\mathrm{fus}}} = (P_{\mathrm{fus}} - P_{\mathrm{fus}}^{\mathrm{eq}})/P_{\mathrm{fus}}^{\mathrm{eq}},\ \varepsilon_{\bar{n}_{\mathrm{e}}} = (\bar{n}_{\mathrm{e}} - \bar{n}_{\mathrm{e}}^{\mathrm{eq}})/\bar{n}_{\mathrm{e}}^{\mathrm{eq}},\ \Delta P_{\mathrm{NB}} = P_{\mathrm{NB}} - P_{\mathrm{NB}}^{\mathrm{eq}},\ \Delta f_{\mathrm{pel}} = f_{\mathrm{pel}} - f_{\mathrm{pel}}^{\mathrm{eq}} \tag{5}$$

Then, calculate the inverse matrix of $\boldsymbol{A}$.

$$\begin{pmatrix} \Delta P_{\mathrm{NB}}/P_{\mathrm{NB}}^{\mathrm{eq}} \\ \Delta f_{\mathrm{pel}}/f_{\mathrm{pel}}^{\mathrm{eq}} \end{pmatrix} = \boldsymbol{A}^{-1} \begin{pmatrix} \varepsilon_{P_{\mathrm{fus}}} \\ \varepsilon_{\bar{n}_{\mathrm{e}}} \end{pmatrix} \tag{6}$$

When performing actual multivariable control, focusing on proportional control, the control (calculation) is performed as follows:

$$\begin{pmatrix} \Delta P_{\mathrm{NB}} \\ \Delta f_{\mathrm{pel}} \end{pmatrix} = \boldsymbol{G}_{\mathrm{p1}} \begin{pmatrix} e_{P_{\mathrm{fus}}} \\ e_{\bar{n}_{\mathrm{e}}} \end{pmatrix} \tag{7}$$

By comparing equations (6) and (7), the multivariable proportional control gain matrix was determined as follows.

$$\boldsymbol{G}_{\mathrm{p1}} = \begin{pmatrix} 0.3147\ [-] & -1.386 \times 10^{-17}\ [\mathrm{MW \cdot m^3}] \\ 0.000\ [\mathrm{s^{-1} \cdot MW}] & 9.388 \times 10\ [\mathrm{s^{-1} \cdot m^3}] \end{pmatrix} \tag{8}$$

To evaluate the validity of the gains, control tests was caried out. The content of the control test are that the target value of the electron density $\bar{n}_{\mathrm{e}}^{\mathrm{target}}$ is reduced while keeping the target value of the fusion power $P_{\mathrm{fus}}^{\mathrm{target}}$ constant. The results of the control test is shown in figure 2.

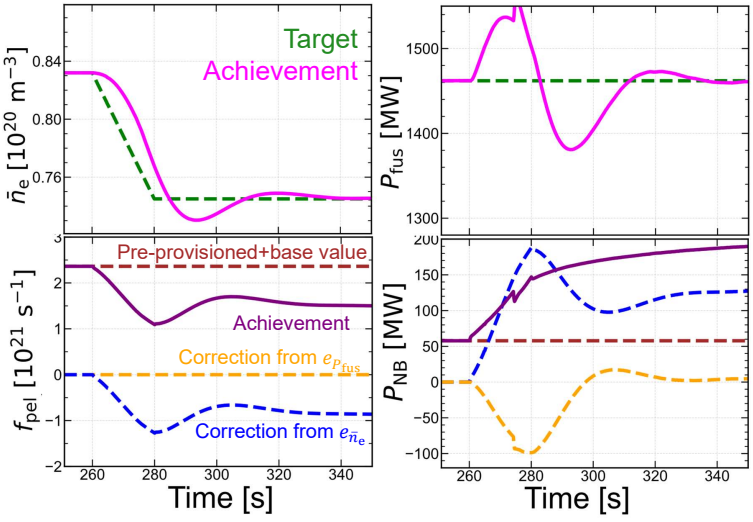

Figure 2: The results of control test using $\boldsymbol{G}_{\mathrm{p1}}$.

Due to G_{12} that corrects P_{NB} from $e_{\bar{n}_\mathrm{e}}$, P_{NB} increases and P_{fus} also increases and fluctuation occurs. Also, the controlled variables do not fully agree with the target value. Therefore, the results of the control test using $\boldsymbol{G}_{\mathrm{p1}}$ indicate that better gains may exist.

2.2 Determining method 2

To find the better gain, another determining method, Ziegler Nicholas' Process Reaction Curve method (ZN method)[4], was attempted. This method is a long established method used in other fields. The procedure of determining gains and time constants are follows:

i. Find the tangent line with the maximum slope on the response curve.
ii. Calculate the slope R of the tangent line and the response delay time L like figure 3.

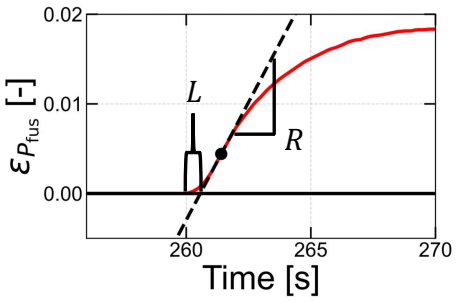

Figure 3: Conceptual diagram for determining R and L values gor using the ZN method.

iii. Determine the gains and the time constants according to the following equation:

$$\boldsymbol{G}_{\mathrm{p}} = \frac{X^{\mathrm{eq}}}{Y^{\mathrm{eq}}} \frac{1.2}{(R/\Delta X)L},$$
$$\tau_{\mathrm{i}} = 2L,\ \tau_{\mathrm{d}} = 0.5L$$

From this method, the calculated gains and time constants are in the following table.

Table 1: Gains and time constants determined by ZN method

	$\boldsymbol{G}_{\mathrm{p2}}$	τ_{i} [s]	τ_{d} [s]
11	1.790 [−]	1.053	0.263
21	0.000 [MW · m^3]	-	-
21	2.766×10^{19} [s^{-1} · MW^{-1}]	3.271	0.818
22	3.033×10^{3} [s^{-1} · m^3]	0.812	0.203

As there was virtually no response of $\bar{n}_\mathrm{e}$ by P_{NB} and R, L could not be determined, the gain was set to zero.

To evaluate the validity of the gains, the same control test in figure 2 was carried out. The results of the control test is shown in figure 4.

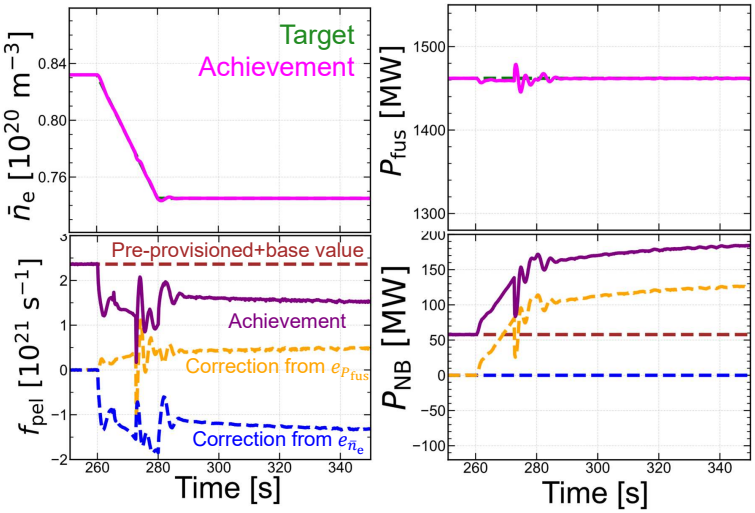

Figure 4: The results of control test using $\boldsymbol{G}_{\mathrm{p2}}$.

As we can see from figure 4, the controlled variables almost agreed with the target value. Therefore, the

gains determined by the ZN method enabled good control performance. However, the values of the manipulated variable fluctuates significantly, so the engineering constraints must be taken into account (Actual manipulated variable may not achieve this fluctuation).

2.3 Differences in determination method

There are two big differences in determination method. First, $\boldsymbol{G}_{\mathrm{p2}}$ (determined by the ZN method) is generally larger than $\boldsymbol{G}_{\mathrm{p1}}$ (using response matrix). This difference arises from their design principles: G_{p1} is determined solely by the final steady-state response ε_Y, whereas G_{p2} is determined by the transient characteristics, specifically the maximum slope R and the delay time L. To clarify the relationship, consider a single-variable control case. The two gains become equal ($G_{\mathrm{p1}} = G_{\mathrm{p2}}$) only when the following condition is satisfied:

$$R \cdot L = 1.2 \cdot \varepsilon_Y \cdot X^{\mathrm{eq}} \tag{9}$$

This equation represents the balance between $R \cdot L$ and ε_Y of the process. In this case, R is relatively small compared to the final steady-state change, causing G_{p2} to be larger than G_{p1} to compensate for the slow initial response. Second, the treatment when there is no (little) response of the controlled variable. In the method using response matrix, no particular mattersto consider. However, in ZN method, when R becomes small, gain becomes large. Therefore, there is a possibility that excessive corrections may be applied to the manipulated variable. This time, the gain derived from the response of $\bar{n}_{\mathrm{e}}$ to P_{NB} was set to zero.

2.4 Considering response delay between the calculation and the actuator's movement

From the results of control test using $\boldsymbol{G}_{\mathrm{p2}}$, we mentioned that the engineering constraints must be taken into account. This time, as a possible constraint, we considered the response delay between the PID calculation and the actuator's response. We modified the logic to enable simulation of actuator response delays, and did the same control tests considering this constraint. The results are shown in Figure 5.

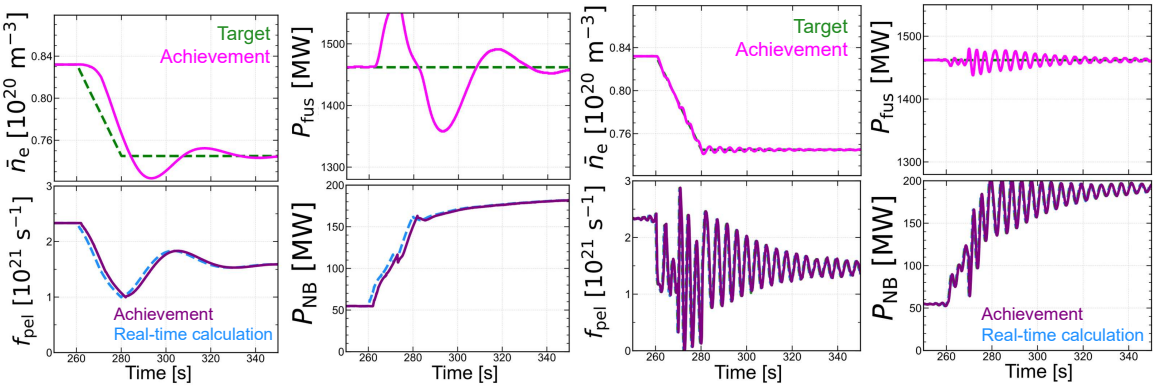

Figure 5: Left: Control test using $\boldsymbol{G}_{\mathrm{p1}}$ considering the delay 2.0 s. Right: Control test using $\boldsymbol{G}_{\mathrm{p2}}$ considering the delay 0.3 s.

When using $\boldsymbol{G}_{\mathrm{p1}}$ and set the delay 2.0 s, the vibration of the controlled variable remains virtually unchanged. However, when usin $\boldsymbol{G}_{\mathrm{p2}}$ and set the delay 0.3 s, a periodic oscillation with a period of approximately 2 seconds appeared. The results suggest that shorter actuator response delays are required for a larger gain (G_{p2}), whereas longer delays are required for a smaller gain (G_{p1}).

3 Summary

In this study, toward multi-variate PID control in JA-DEMO, we compared methods for determining control gains using TOTAL. We set P_{fus} and $\bar{n}_{\mathrm{e}}$ as the controlled variables, and P_{NB} and f_{pel} as the manipulated variables. We calculated the PID gains $\boldsymbol{G}_{\mathrm{p}}$ and time constants τ_{i}, τ_{d} using two different methods based on step responses. First, the method using response matrix can determine all gains mechanically regardless of the magnitude of the step response, though it still requires empirical tuning for the time constants. Second, while the ZN method showed good overall control, we observed significant deviations of the manipulated variables. We also considered response delay between the control calculation and the actuators movement. Results indicate that a larger gain ($\boldsymbol{G}_{\mathrm{p2}}$) is appropriate to a shorter delay, while a smaller gain ($\boldsymbol{G}_{\mathrm{p1}}$) is appropriate to a longer delay.

As the next step, we plan to determine the optimal gains that specifically match the expected response delays

of actual hardware actuators.

Acknowledgment

This work was supported by the Research and Development Collaboration on DEMO Reactors of QST.

References

[1] Working group report on Diagnostics & Control for fusion DEMO, Joint Special Design Team for Fusion DEMO, September 2023.
[2] Y. Sakamoto et al., 25th IAEA Int. Conf. on Fusion Energy(St. Petersburg, Russia, 2014), FIP/3-4Rb.
[3] K. Yamazaki and T. Amano, Nucl. Fusion 32, 633 (1992).
[4] J. G. Ziegler and N. B. Nicholas, Trans. ASME. 1942, 64(8).

Study on Image Reconstruction of Lensless Microwave Holography in a Linear Plasma Device

Yuya Ohta, Mayuko Koga

University of Hyogo

1. Research Background

In fusion research, microwave diagnostics are one of the primary methods for observing plasmas [1]. In microwave diagnostics, microwaves are injected into the plasma, and the intensity and phase of the reflected waves are measured, making this technique suitable for determining positions along the line of sight. However, conventional microwave diagnostics do not provide sufficient spatial resolution [2].

To address this issue, we propose lensless microwave holography. Compared with conventional microwave holography employing optical systems which consisted of lens or mirrors, the lensless approach offers a wider field of view. However, this approach requires complex reconstruction calculations, and solving them mathematically results in high computational cost [3].

Therefore, we propose an image reconstruction method based on machine learning. In previous studies, a corrugated planar mirror was used as the target object [4]. In this study, we use simulation data from a linear plasma device (PANTA) provided by Professor Naohiro Kasuya of the Research Institute for Applied Mechanics, Kyushu University, as the target object, and attempt to reconstruct plasma density distribution images of argon (Ar) and helium (He) from the received microwave data.

2. Method

The procedure for generating training data for machine learning is described below. Fig.1 shows a schematic overview of the procedure used to construct plasma density distribution images of Ar and He, which serve as the target objects.

First, plasma data at the cutoff density were extracted from linear plasma simulation data. Spatial windows referred to as probes were arranged at the plasma surface. These proves were set 300 mm from the microwave antenna array. These probes were set along the plasma surface, with a total of 99 probes. For each probe, the distance between each probe and the plasma cutoff surface was calculated.

This procedure was repeated at 294 equally spaced time steps, resulting in a total of 29,106 plasma density distribution images for Ar and He.

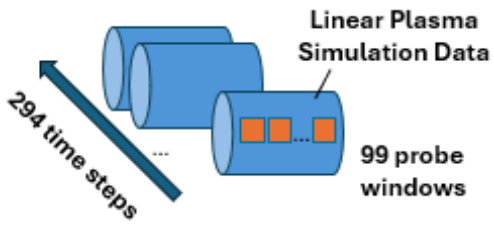

Fig.1 Schematic overview of the procedure for generating plasma density distribution images

In microwave holography, the received signal g can be expressed by the equation $Hf = g$, where H denotes the propagation function and f represents the scattering rate, defined as the reflectivity $f(x, y, z)$at a point (x, y, z). Using this equation, electromagnetic wave calculations were performed, and complex microwave amplitude images were generated as received data from plasma density distribution images. These data were used as training data for the learning process.

In this study, a convolutional neural network (CNN) was employed as the learning model. An example of the model architecture is shown in Fig. 2. The input consists of complex microwave amplitude images; since the data are complex-valued, they were provided as two-channel inputs corresponding to the real and imaginary parts. The output is the plasma density distribution image.

In this work, training was performed while varying the filter size and the number of convolutional layers: one layer with a 5×5 filter, one layer with a 7×7 filter, and one to four layers with 3×3 filters. The reconstruction accuracy was compared using two error metrics: the root mean square error (RMSE) and the mean absolute error (MAE).

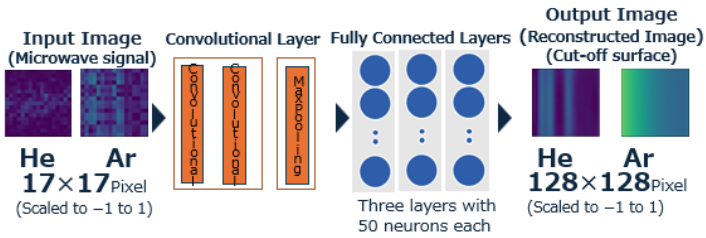

Fig.2 Schematic diagram of the CNN model

3. Results

Fig.3 shows the error values obtained by varying the filter size and the number of layers while keeping the receptive field the same, and Fig. 4 shows the error values obtained by varying the number of layers with the same filter size. The error bars represent the standard deviation of the error values obtained from training on five different datasets, which were created by changing the assignment of the training, validation, and test data from the ground-truth dataset.

In all cases, both RMSE and MAE were consistently smaller for Ar than for He. Furthermore, when comparing configurations with the same receptive field—namely, one layer with a 5×5 filter versus two layers with 3×3 filters, and one layer with a 7×7 filter versus three layers with 3×3 filters—the error values for Ar were lower when multiple layers with smaller filters were stacked, whereas little difference was observed for He. In addition, the lowest error was obtained with four layers of 3×3 filters for Ar, while three layers of 3×3 filters yielded the lowest error for He.

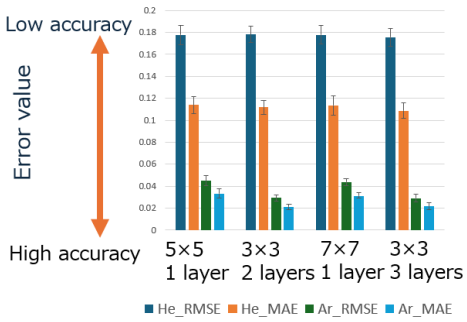

Fig.3 Error values obtained by varying the filter size and the number of layers with the same receptive field

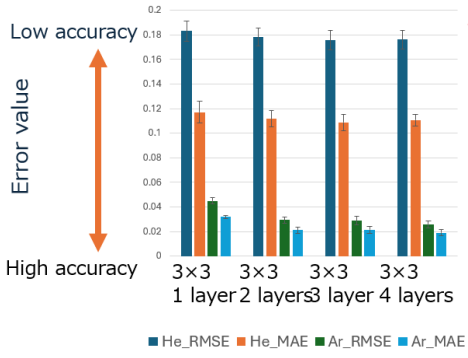

Fig. 4. Error values obtained by varying the number of layers with the same filter size

Figure 5 shows the reconstructed images for Ar, and Fig. 6 shows the reconstructed images for He. In the reconstructed images of Ar, it can be seen that variations in brightness and gradation are reproduced with high accuracy. In contrast, the reconstructed images of He are generally darker than the corresponding ground-truth images. Furthermore, the positions and the number of stripe-like patterns are not correctly reproduced, and lines that are partially interrupted in the ground-truth images are reconstructed as continuous lines extending from top to bottom. As a result, accurate image reconstruction could not be achieved for He in this study.

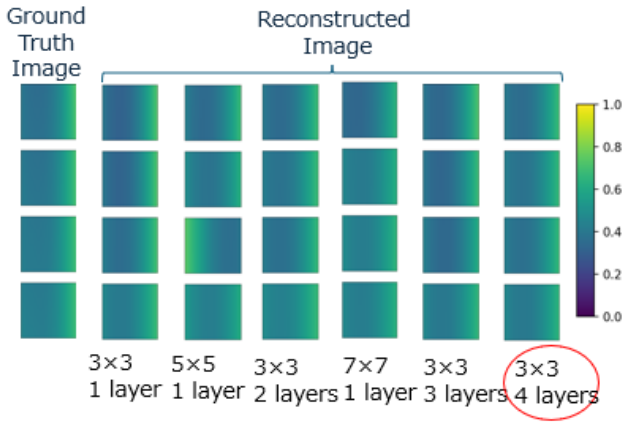

Fig. 5. Reconstructed images of Ar

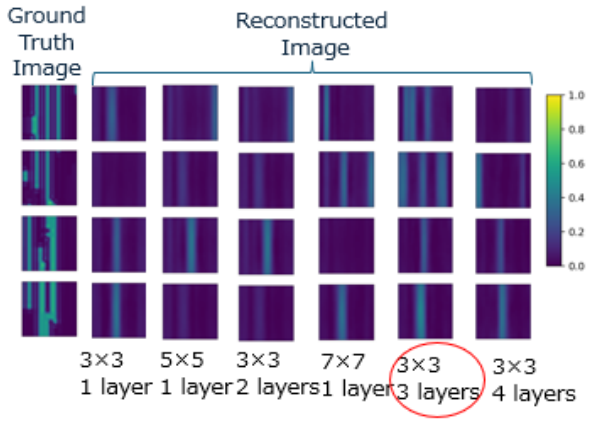

Fig. 6. Reconstructed images of He

4. Data analysis

To investigate the reason why high-accuracy image reconstruction could not be achieved for He, the plasma density distribution images used as the training data were analyzed. First, histograms of pixel values for each pixel are shown in Fig. 7. Most of the Ar data are distributed in the range of pixel values from 0.3 to 0.9 and exhibit a distribution similar to a Gaussian. In contrast, most of the He data are concentrated near a pixel value of 0, followed by a secondary distribution around a pixel value of approximately 0.5. This indicates that the He data are biased toward darker values.

In this study, the mean squared error (MSE) was used as the loss function in the machine learning model, which causes the reconstructed images to be biased toward the mean of the training data. As a result, the reconstructed images for He are considered to be generally darker than the corresponding ground-truth images.

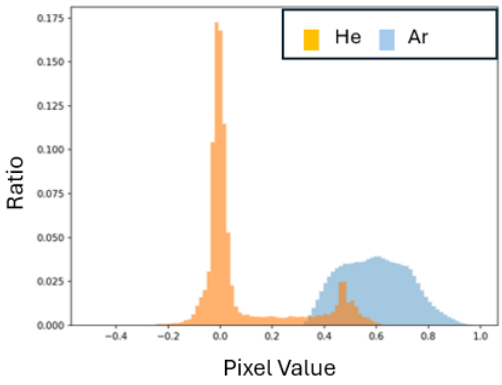

Fig. 7. Histogram of pixel values for each pixel

Next, the pixel-wise variance of pixel values for He and Ar is shown in Fig. 8. The variance for Ar is generally small, with only slight variations observed near both edges. In contrast, the variance for He is significantly larger and strongly dependent on the position along the horizontal. These results indicate that the He data exhibit greater pattern diversity than the Ar data, making the learning task more challenging.

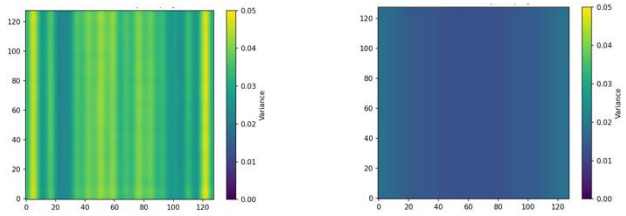

Fig. 8. Pixel-wise variance of pixel values for He (left) and Ar (right)

5. Conclusion and future work

In this study, it was found that, for Ar, stacking smaller filters improved the reconstruction accuracy even when the receptive field was kept the same, whereas for He, the accuracy showed little dependence on the filter size or the number of layers. The highest accuracy was achieved with three layers of 3×3filters for He and four layers of 3×3 filters for Ar.

Although high-accuracy reconstruction of plasma density distribution images was successfully achieved for Ar, several issues were observed for the reconstructed images of He, such as discrepancies in the positions of stripe-like patterns, darker reconstructed patterns compared to the ground-truth images, and difficulty in reproducing partially interrupted lines.

To investigate the causes of these issues, the training data were analyzed. The results showed that, for Ar, the pixel values follow a Gaussian-like distribution, whereas for He, the pixel values are biased toward a smaller range. In addition, while the pixel-wise variance is small for Ar, it is large for He, indicating greater diversity in the He data.

As future work, in order to achieve high-accuracy reconstruction of He plasma density distribution images, several approaches can be considered. One approach is to mitigate the bias in the training data by applying weighting to brighter data. Another possible approach is to employ different model architectures, such as encoder–decoder–type networks, for training.

References

[1] A. Ejiri, “Microwave Reflectometry for Plasma Diagnostics,” Journal of the Plasma and Fusion Research, **79**, (2003) (in Japanese).

[2] H. Tsuchiya et al., Plasma Fusion Res. **14**, 3402146 (2019).

[3] R. Takenaka, “Three-dimensional electromagnetic calculations for image reconstruction in microwave holography,” Master’s thesis, Graduate School of Engineering, University of Hyogo, (2021) (in Japanese).

[4] R. Manabe, “Study on lensless millimeter-wave imaging reconstruction using machine learning,” Master’s thesis, Graduate School of Engineering, University of Hyogo, (2022) (in Japanese).

Estimation of Fast Ion Density Distribution in Fusion Plasma Using FIDASIM Data and CNN

Hiroki Nakata[1], Mayuko Koga[1], Yuya Ohta[2], Yuto Sugii[2], Hiroyuki Yamaguchi[3,4], Yasuko Kawamoto[3], Hideo Nuga[3] and Masaki Osakabe[3,4]

[1] Graduate School of Engineering, University of Hyogo
[2] Faculty of Engineering, University of Hyogo
[3] National Institute for Fusion Science
[4] The Graduate University for Advanced Studies, SOKENDAI

1. Introduction

In fusion reactors, burning plasma is heated by high-energy alpha particles generated by the fusion reaction of deuterium and tritium inside the plasma. The confinement of fast ions is necessary for stable heating. As a method for measuring the spatial and velocity information of fast ions, FIDA (Fast Ion D-Alpha) measurement, which utilizes light generated by the charge exchange reaction of fast ions (Fig. 1), is attracting attention.

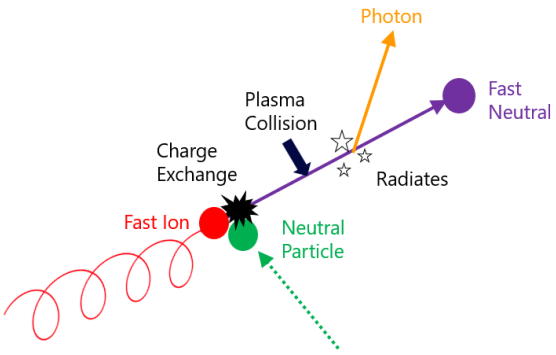

Fig. 1 Illustration of charge exchange reaction.

In the spectral analysis of FIDA measurement, measured spectrum can be compared with a calculated spectrum using a simulation (FIDASIM) by inputting plasma parameters. By repeating this process changing the input parameters until both spectra match, realistic fast ion distribution can be estimated. In this study, aiming to speed up data analysis for FIDA, we attempted to directly estimate the fast ion density distribution from spectral data using machine learning.

2. Experimental Methods and Results

Spectroscopic data from FIDASIM and fast ion density distributions calculated assuming the FIDA geometry in the Large Helical Device (LHD) at National Institute for Fusion Science (NIFS) were used as training data. A Convolutional Neural Network (CNN) was used as the machine learning model to construct a network that reconstructs the spatial distribution of fast ion density from the input FIDASIM spectrum. ReLU was used as the activation function. Model performance was evaluated by varying the number of convolutional layers (kernel size 3×1) from 1 to 5 layers. RMSE (Root Mean Square Error) and MAE

(Mean Absolute Error) were used as evaluation metrics. Additionally, MAE and RMSE normalized by the maximum value of each data were defined as MAE_{norm} and $RMSE_{norm}$. The evaluation metrics for different numbers of convolutional layers are shown in Fig. 2. It can be seen that the model accuracy is highest with of 4 layers.

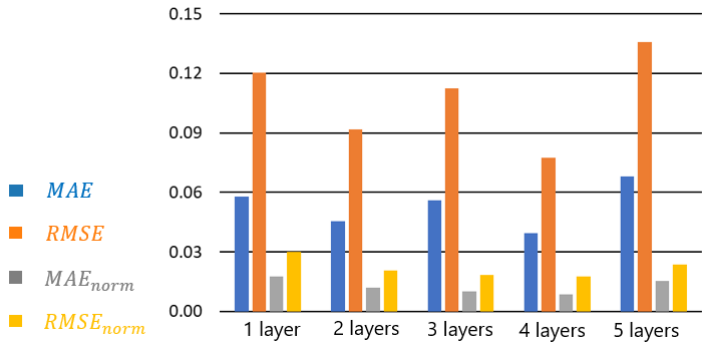

Fig. 2 Evaluation metrics versus the number of convolutional layers.

Figure 3 shows typical ground truth and predicted fast ion density distributions at various toroidal angles ϕ using the 4-layer convolutional model. It is clearly seen that the model successfully captures the three-dimensional shape of the plasma in the LHD.

Figure 4 shows a comparison between the ground truth and predicted fast ion density distributions at $\Phi=0$ for various density cases. From Fig. 4, it can be seen that the trends in the distributions are successfully predicted. However, the predicted densities tend to be lower than the ground truth data. This is likely due to bias in the training data.

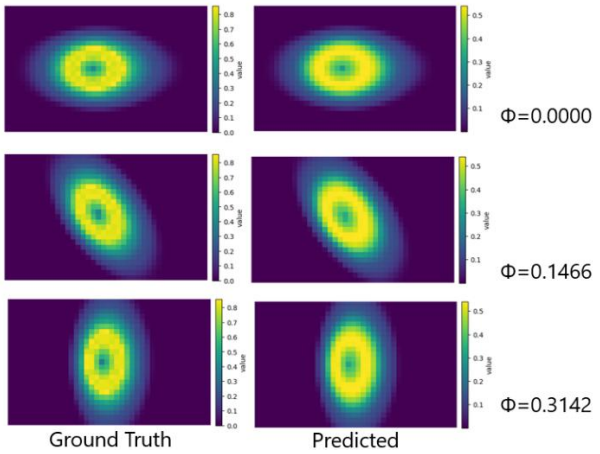

Fig. 3 Typical ground truth and predicted fast ion density distributions at various toroidal angles.

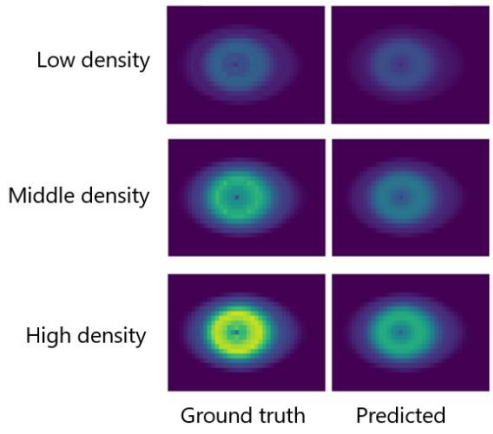

Fig. 4 Ground truth and predicted fast ion density distribution at $\Phi=0$ for various density cases.

3. Future Work

In future work, we aim to mitigate data imbalance to improve reproduction accuracy, particularly in the region near the magnetic axis. Furthermore, we plan to extend the framework to estimate fast ion distributions in velocity space.

計測シミュレーションを利用した PCI 信号からの乱流スペクトル再構築

Reconstruction of Turbulence Spectrum from PCI Signals by Using Numerical Diagnostics

Lin Hanqing[1], Naohiro Kasuya[1,2], Kenji Tanaka[1,3]

[1]IGSES, Kyushu Univ., [2]RIAM, Kyushu Univ., [3]NIFS.

1 Research Background and Objective

Phase Contrast Imaging (PCI) is one of the key diagnostics for plasma turbulence [1],[2], but its line-integrated nature compresses 3D information into a 2D signal. In JT-60SA, the magnetic field direction rotates by over 90 degrees along its tangential line of sight, making traditional inverse techniques for profile reconstruction to be challenging [3]. Machine Learning (ML) is a powerful tool to retrieve radial profiles from the integrated signals [4]. Developing such an ML algorithm requires a massive training dataset. First-principle simulations for tokamaks can produce 3-D patterns of turbulent fluctuations, which can be used as the training dataset. The objective of this work is to validate the forward model for evaluating PCI signals numerically by using high-fidelity simulation data. By scanning turbulence-driving parameters, we verify whether this synthetic diagnostic correctly captures the spectra in the real geometry, serving as a benchmark for future development of reconstruction tools from PCI signals.

2 PCI Simulation: Forward process for obtaining observation signals

We have constructed a numerical scheme for PCI simulation [5]. This forward modeling calculates the observed signal from the PCI measurement by line-integration of density fluctuations (Figure 1). The 3D density fluctuation field, ñ, is calculated by gyrokinetic code GENE [6], mapped onto the realistic JT-60SA magnetic configuration provided by TASK/EQU [7]. As shown in Figure 1, the simulated turbulence by the flux-tube model is typically localized around specific flux surfaces with clean spectral features, representing an idealized physical state. Then line integration generates a 2D simulated PCI detector signal, $I(x,y)$, through a synthetic diagnostic routine [3], [5]. Finally, to analyze the spatial characteristics, we apply a 2D Fast Fourier Transform (FFT) to $I(x,y)$. This yields the 2D wavenumber spectrum, $S(k_x, k_y)$, which is the primary statistical quantity for verifying the forward model's sensitivity. Noted that the frequency resolution of the PCI diagnostic is determined by the detector's physical width (L_y) and normalization using the ion Larmor radius ρ_i:

$$k_y \rho_i = \left(j \frac{2\pi}{L_y}\right) \times \left(\frac{\sqrt{2T_{\mathrm{ref}} m_{\mathrm{ref}}}}{eB_{\mathrm{ref}}}\right) , \quad (1)$$

where j is the harmonic index, T_{ref}, m_{ref}, and B_{ref} are the reference temperature, ion mass, and magnetic field, respectively.

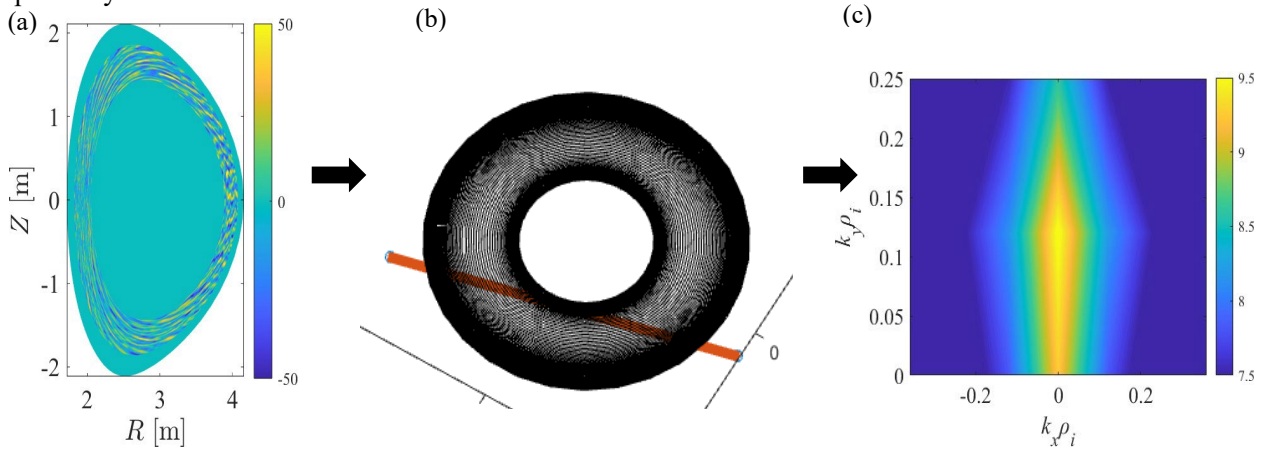

Figure 1. PCI Forward Simulation Workflow. (a)Simulation data of 3D fluctuation field are used for (b)obtaining the PCI signal by line-integration, from which (c)physical quantities (e.g. 2D density fluctuation) are evaluated.

3 Analysis of Saturated Turbulence

To validate response of the forward model to physical parameter changes, we performed nonlinear simulations

comparing a Strong Drive case (R/L_T=7.0) with a Weak Drive case (R/L_T=5.0). In the simulation analysis, the normalized temperature gradient is defined as R/L_T, where R is the major radius and $L_T = -(\nabla T/T)^{-1}$ is the temperature gradient scale length.

During the initial analysis of the Weak Drive case (R/L_T=5.0), a sharp spectral peak was observed at $k_y\rho_i \approx 0.275$. Figure 2(a) presents the "Full" fluctuation field mapped on the poloidal cross-section. A "Bandpass" filtered field (retaining only components with $k_y\rho_i \in [0.2,0.35]$) reproduces the primary eddy structures observed in the Full field, whereas the "Residual" field (Full minus Bandpass) shows no coherent structures. This confirms that the mode at $k_y\rho_i \approx 0.275$ indeed dominates the spatial turbulence structure in the Weak Drive case.

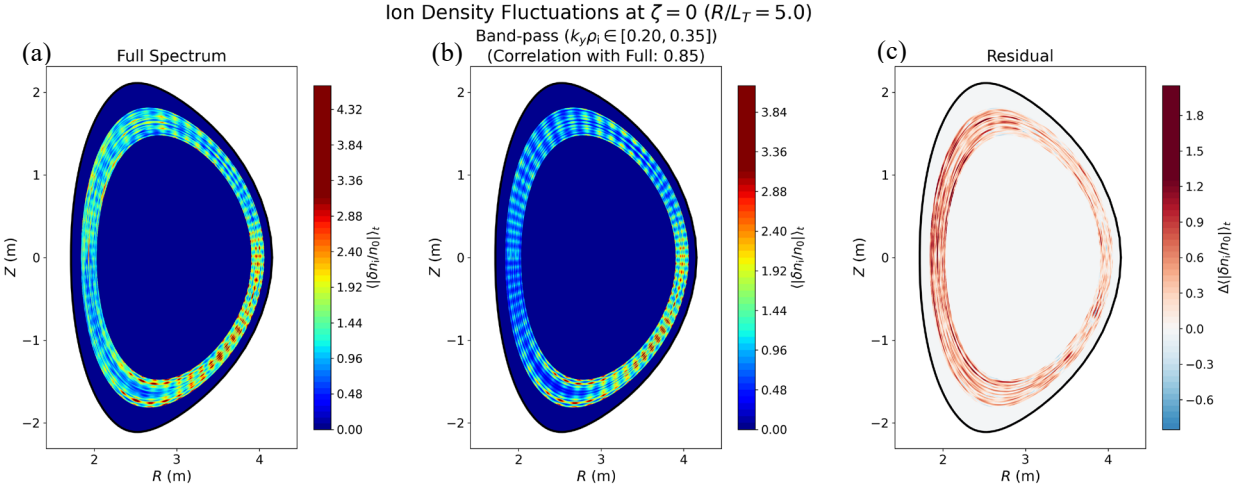

Figure 2. Spatial distribution of ion density fluctuations on the poloidal plane ($\zeta = 0$). (a) Full fluctuation field, (b) Band-pass filtered field ($k_y\rho_i \in [0.20,0.35]$) and (c) Residual field (Full minus Band-pass) are shown.

We compare the GENE spectra with the synthetic PCI spectra. Figure 3 compares the density fluctuation power in the local poloidal wavenumber spectra, $S(k_y)$, in the flux coordinates used in the GENE simulations. The Strong Drive case (red) shows significantly higher power (1-2 orders of magnitude) than the Weak Drive case (blue). In addition, a distinct shift is observed; the spectral peak moves from $k_y\rho_i \approx 0.28$ (Weak) to a lower wavenumber region (Strong), indicating that dominant eddy scales increase by an inverse cascade process under stronger instability driving.

Next, we processed these fields through the PCI synthetic diagnostic. To evaluate the observed energy, we integrated the 2D PCI spectrum along the radial wavenumber k_x:

$$S(k_y) = \int \left|\tilde{n}(k_x, k_y)\right|^2 dk_x \ , \qquad (2)$$

where $\tilde{n}(k_x, k_y)$ is the Fourier transform of the density fluctuation (Figure 4). This integration approach captures the total fluctuation power at a given poloidal scale, averaging out radial structural variations.

Comparison between Figures 3 and 4 represent the characteristic features are captured in the PCI synthetic diagnostic signals. In the PCI integrated spectrum (Figure 4), the Strong Drive case consistently exhibits higher power than the Weak Drive case. The distinct peak in the Weak Drive case and the trend of the spectral peak shifting towards the lower wavenumber region are qualitatively preserved in the synthetic observation. However, the exact shape of the spectrum is modulated. The sharp feature observed in Figure 4 appears smoothed in the PCI observation. This is mainly given by limited spatial resolution with a finite number of the detectors. As discussed in Ref. [3], the PCI signal is a superposition of fluctuations from various radial locations weighted by the optical geometry. This line-integration effect also distorts spectral features such as the decay rate and peak sharpness.

4 Summary

In summary, we have built and validated a forward model of the PCI observation for JT-60SA. The simulation results confirmed that the synthetic PCI signal effectively detects macroscopic shifts in turbulence scales caused by changes in driving gradients. This validates the forward model as a reliable tool for generating input-output pairs.

Future work will focus on constructing a large-scale training database to solve the inverse problem using Deep Unfolded Networks. To overcome the high computational cost of first-principle simulations as nonlinear simulation with GENE, we will develop computationally efficient "toy models" (stochastic turbulence generators). Crucially,

these stochastic models will be employed for data augmentation to generate synthetic turbulence profiles with broader spatial distributions and multi-scale background noise. This strategy aims to bridge the gap between idealized simulations and complex experimental environments, ensuring the ML model is robust enough to reconstruct radial turbulence profiles from real PCI measurements in JT-60SA.

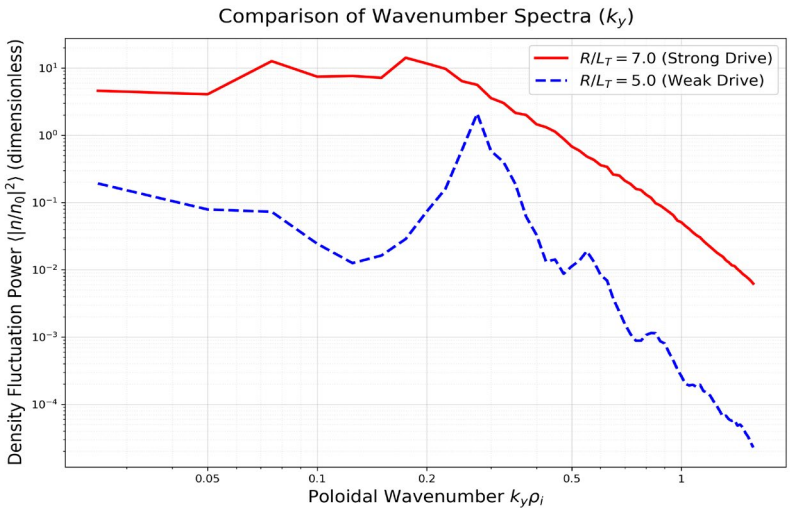

Figure 3. Local poloidal wavenumber spectra $S(k_y)$ in the flux coordinates of GENE.

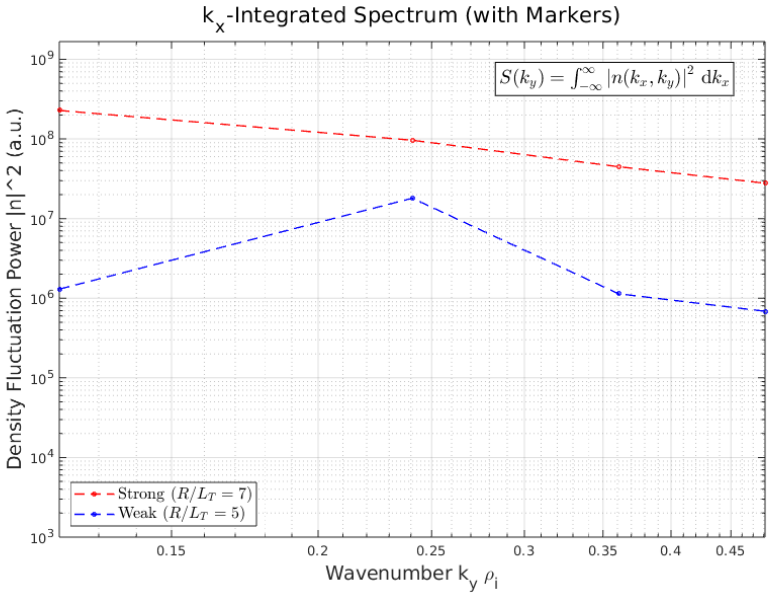

Figure 4. Wavenumber spectra derived from simulated PCI signals in the Cartesian coordinates of the observation line of the sight.

References

[1] S. Coda, *et al*, Nucl. Fusion **61**, 106022 (2021).
[2] K. Tanaka, *et al.,* Rev. Sci. Instrum. **79**, 10E702 (2008).
[3] N. Kasuya, *et al*., Nucl. Fusion **58**, 106033 (2018).
[4] L. van Leeuwen, *et al*., Plasma Phys. Control. Fusion **67**, 025024 (2025).
[5] K. Kuwamiya, *et al.*, Proc. 22th BPSI meeting (Kasuga, 2024) 1-8.
[6] F. Jenko, *et al*., Phys. Plasmas **58**, 1904 (2000).
[7] https://bpsi.nucleng.kyoto-u.ac.jp/task/